



Multiscale assessment of Indian monsoon rainfall using ICON and CMIP6 model simulations

Samir Pokhrel¹, Verma Utkarsh^{1,2}, Patita Kalyana Sahoo^{1,3}, Praveen Pothapakula⁴, Anusha Sunkisala⁵, Nishant Gautam^{1,3}, Kolady P. Pribin^{1,3}, Shivamurthy Yashas^{1,2}, Hemant Chaudhari¹, Archana Rai¹, Hasibur Rahaman⁶, Andreas F. Prein⁴, Anurag Dipankar⁴, and Subodh K. Saha¹

¹Indian Institute of Tropical Meteorology, Pune, India

²Savitribai Phule Pune University, Pune, India

³Academy of Scientific and Innovative Research, Ghaziabad, India

⁴Institute for Atmospheric and Climate Science, ETH Zürich, 8092 Zurich, Switzerland

⁵Independent Researcher, Zürich, Switzerland

⁶Indian National Centre for Ocean Information Services, Ministry of Earth Sciences, Hyderabad, India.

Correspondence: Samir Pokhrel (samir@tropmet.res.in)

Abstract.

Indian Summer Monsoon (ISM) rainfall is organized across multiple timescales, from diurnal convection to synoptic disturbances, intraseasonal oscillations, and the seasonal mean. Climate models often show different levels of skill at each of these timescales, raising an important question: how do scale-dependent biases shape overall monsoon variability? Here, we assess a medium-resolution (40 km), non-hydrostatic global model (ICON) together with five hydrostatic CMIP6-class models (CNRM, MPI, GFDL, MIROC6, and IITM-ESM; 50–190 km resolution). All simulations are evaluated in AMIP configuration against high-resolution IMERG observations during 1998–2014, allowing isolation of atmospheric sources of rainfall bias. Rainfall errors are strongly scale-dependent and exhibit clear land–ocean contrasts. At the diurnal scale, ICON reproduces amplitudes over the continent with a relatively small bias (~5–10%), whereas MPI overestimates land diurnal amplitude by more than 150% with premature triggering. The CNRM and GFDL show early daytime convection and weak nocturnal rainfall, while MIROC6 and IITM-ESM exhibit reduced diurnal amplitude linked to convective and resolution limitations. Over the Bay of Bengal, ICON overestimates diurnal amplitude (~60%) and variance (~180%), whereas CMIP6 models underestimate nocturnal oceanic variability (amplitude < 40%, variance < 60%). At synoptic timescales (2–7 days), models differ in their ability to sustain organized monsoon disturbances. ICON and GFDL maintain realistic spatial structure with moderate suppression, while MPI underestimates synoptic variance by up to ~70–80%. Other models either has weakened synoptic activity or redistribute variability toward intermediate (10–20 day) bands. Across the ensemble, the 20–100-day intraseasonal band is systematically underestimated (by ~30–60%) in the AMIP framework, suggesting that coupled ocean–atmosphere feedbacks, among other factors, contribute to maintaining monsoon intraseasonal oscillations. Seasonal rainfall patterns reflect the combined effect of these multiscale biases. Models that maintain a balanced variance distribution across diurnal, synoptic, and intraseasonal bands show improved seasonal structure, whereas distortions at intermediate frequencies contribute to amplitude and migration errors. These results indicate that credible monsoon simulation depends not only on seasonal-mean accuracy



but also on physically consistent variability across timescales. A scale-aware diagnostic framework is therefore essential for improving convective triggering, mesoscale organization, boundary-layer processes, and air–sea coupling in climate models.

25 1 Introduction

Accurate forecasting of precipitation over the Indian subcontinent has long remained an enduring scientific challenge, with growing demand for skillful predictions not only at all-India level but scaling down till block level. Achieving such high spatial fidelity in rainfall prediction requires forecast models to faithfully reproduce all the fundamental scales of variability of the Indian summer monsoon, ranging from the diurnal convective cycle to synoptic disturbances, intraseasonal oscillations (ISOs), and the seasonal mean rainfall. These interacting scales form the backbone of monsoon dynamics, collectively governing how convection initiates, organizes, and propagates across the subcontinent (Webster et al., 1998; N., 2005). Their interplay determines not only the timing and intensity of rainfall, but also the limits of its predictability on different timescales (e.g. Turner and Annamalai, 2012). Yet, despite remarkable progress in model physics, resolution, and data assimilation over the past decades, systematic errors in simulating precipitation remain pervasive across generations of global climate models (Sperber et al., 2013), particularly in regions such as Central India (CI) and Bay of Bengal (BoB) where multiscale convective coupling and ocean–land–atmosphere interactions dominate.

Rainfall variability during the Indian summer monsoon arises from a hierarchy of interacting physical modes. At the shortest timescale, the diurnal cycle represents one of the most fundamental features of tropical convection, exerting strong control on the timing and organization of rainfall over both land and ocean (Johnson, 2011). Over India, the diurnal cycle is strongly modulated by orography, land–sea thermal contrasts, and large-scale circulation, leading to pronounced regional heterogeneity that has recently been observed to experience significant spatial and temporal phase shifts (e.g. Basu, 2007; Sen Roy and Balling Jr., 2007; Sahany et al., 2010; Chutia et al., 2025, etc.). The next tier of variability, the synoptic disturbances on 2–7-day timescales, comprises monsoon low-pressure systems (LPS) that form primarily over the BoB and propagate north-westward, delivering substantial rainfall to CI (Godbole, 1977; Sikka, 1977; Patwardhan et al., 2020; Hunt and Turner, 2022). These systems are dynamically linked to moist baroclinic instability within the monsoon trough, energized by strong meridional shear and cyclonic vorticity (Shukla, 1987; Goswami et al., 1980; Mak, 1987). At longer timescales, the ISOs emerge as dominant modes of low-frequency variability, characterized by quasi-periodic fluctuations in convection and rainfall on 10–20-day and 30–60-day bands (Krishnamurti and Bhalme, 1976; Yasunari, 1979; Sikka and Gadgil, 1980). Together, these two modes account for nearly 90% of the total intraseasonal variability in monsoon rainfall (Annamalai and Slingo, 2001). The 30–60-day mode, typically originates over the equatorial Indian Ocean and propagates northward, while the 10–20-day mode often initiates over the South China Sea and propagates north-westward (Webster et al., 1998; Wang, 2006). Collectively,



these diurnal, synoptic, and intraseasonal modes form an interconnected cascade that shapes the structure, evolution, and predictability of the Indian summer monsoon (Krishnamurti and Subrahmanyam, 1982).

Among these multiscale physical modes, the diurnal cycle of precipitation serves as a fundamental testbed for assessing a model's ability to reproduce key convective and radiative processes (Lin et al., 2000; Trenberth et al., 2003; Dai and Trenberth, 2004, etc.). Despite major progress across generations of the Coupled Model Intercomparison Project (CMIP), models continue to exhibit persistent biases in simulating tropical diurnal rainfall. Evaluations of CMIP6 models have revealed that the timing of peak rainfall is typically 3–5 hours too early over land and 1–2 hours too early over oceans compared with high-quality satellite and gauge observations (Tang et al., 2021, 2022; Christopoulos and Schneider, 2021). Over land, many models exhibit premature initiation of convection, producing rainfall peaks several hours earlier than observed and leading to overly frequent but weak precipitation, the so-called "drizzling bias" (Chen et al., 2021). This behaviour arises from the inability of conventional cumulus parameterization schemes to realistically simulate the morning growth of the non-precipitating convective boundary layer (Betts and Jakob, 2002; Bechtold et al., 2004) and the associated buildup of convective available potential energy (CAPE; Folkins et al., 2014; Rio et al., 2009; Tawfik et al., 2017). Over oceans, the diurnal amplitude is often underestimated due to the absence of subdaily air–sea coupling and diurnal sea surface temperature (SST) variability over the Indian subcontinent (Baranowski et al., 2019; Peng and Chen, 2024), these problems are amplified by strong land–sea thermal contrasts and orographic influences, where models often fail to reproduce the observed afternoon peaks and propagating MCSs over the BoB (Kilpatrick et al., 2017; Seo et al., 2014). Importantly, these deficiencies extend beyond the diurnal scale. CMIP6 models continue to underrepresent the intensity and organization of monsoon LPSs and ISOs (Sperber et al., 2013; Konda and Vissa, 2022; Jiang et al., 2020). Many models struggle to simulate the amplitude, northward propagation, and phase coherence of the 10–20-day and 30–60-day ISOs, indicating systematic errors in convective–dynamical coupling across scales (Rajendran et al., 2022). These results suggest that precipitation biases are not isolated at individual time scales but may reflect misrepresentation of scale interactions and convective organization. A systematic multiscale evaluation is therefore essential to determine whether model errors arise independently at each temporal mode or cascade across interacting scales

Accurate simulation of monsoon rainfall fundamentally depends on the representation of vertical motion and its coupling with moist convection. In the tropics, vertical velocity governs moisture convergence, buoyancy generation, and latent heat release, thereby controlling the initiation, intensity, and organization of deep convection (Emanuel, 1994; Houze Jr., 2004). The vertical momentum equation may be expressed as

$$\frac{Dw}{Dt} = -\frac{1}{\rho} \frac{\partial p'}{\partial z} + B + F, \quad (1)$$

where Dw/Dt denotes the vertical acceleration, ρ is the air density, p' represents the perturbation pressure, B denotes buoyancy, and F represents subgrid-scale forcing terms. This formulation highlights the central role of vertical acceleration in convective dynamics. In hydrostatic general circulation models (GCMs), vertical motion is diagnostically constrained under the hydrostatic approximation, which filters vertical acceleration and may limit the representation of mesoscale convective circulations and gravity-wave–convection interactions. In contrast, non-hydrostatic dynamical cores explicitly solve the vertical momentum equation, allowing a more dynamically consistent treatment of vertical accelerations associated with organized convection



and mesoscale systems (Sato et al., 2008; Stevens et al., 2019). Given that monsoon precipitation variability across diurnal to intraseasonal time scales is tightly linked to convective organization, the fidelity of vertical motion representation may substantially influence simulated multiscale rainfall characteristics however, improvements in physical parameterizations and model coupling are equally important.

90 Recent advances in atmospheric modelling include the development of the ICOSahedral Nonhydrostatic (ICON) model (Zängl et al., 2015; Dipankar et al., 2026), which employs a non-hydrostatic dynamical framework. While convection remains parameterized at typical climate-model resolutions, the explicit treatment of vertical acceleration and improved dynamical consistency may influence the simulation of tropical precipitation variability. A concise assessment of whether such dynamical formulation translates into improved multiscale precipitation representation over the Indian monsoon region remains lacking.
95 Therefore, we employ the ~ 40 km global configuration of ICON model as a practical test case to evaluate the added value of non-hydrostatic dynamics for simulating Indian summer monsoon variability. At ~ 40 km resolution, ICON occupies an important intermediate regime between traditional hydrostatic climate models and emerging convection-permitting global simulations. It allows explicit representation of key mesoscale features while remaining computationally feasible for multi-year integrations, thereby providing an ideal framework to assess whether non-hydrostatic dynamics improve the simulation of
100 monsoon variability across scales.

In this study, we evaluate precipitation characteristics across diurnal, synoptic, intraseasonal, and seasonal scales using simulations from ICON and selected CMIP6 atmospheric models, including CNRM-CM6-1-HR, MPI-ESM1.2-HR, GFDL-CM4, MIROC6, and the IITM Earth System Model (IITM-ESM). All simulations are analysed in their Atmospheric Model Inter-comparison Project (AMIP) configuration to compare monsoon convection under prescribed sea surface temperature boundary
105 conditions. The novelty of this work lies in providing a unified, scale-aware assessment of how a medium-resolution non-hydrostatic global model performs relative to state-of-the-art hydrostatic CMIP6 models in simulating the full spectrum of Indian monsoon rainfall variability, with particular emphasis on identifying scale-dependent strengths, deficiencies, and the consistency of model errors across the temporal hierarchy across key monsoon subregions. The paper is organized as follows: Section 2 describes the datasets, models, and experimental design. Section 3.1 evaluates the diurnal characteristics of monsoon
110 rainfall, while Section 3.2 examines synoptic and intraseasonal variability using variance and spectral diagnostics. Section 3.3 shows the error in the seasonal scale and also assess scale-wise error characteristics across models. Finally, Section 4 summarizes the main findings and discusses their implications for future non-hydrostatic global modelling of the Indian monsoon.

2 Data and Methodology

2.1 Observation

115 2.1.1 IMERG

Precipitation observations are obtained from the Integrated Multi-satellite Retrievals for the Global Precipitation Measurement (IMERG) Version 07 Final Run product (Huffman et al., 2023), spanning 1998-2023. IMERG is developed under the Global



Precipitation Measurement (GPM) mission and provides globally consistent, gauge-adjusted precipitation estimates by merging passive microwave observations from a constellation of ten satellites including dual-frequency precipitation radar, as well as a multi-channel GPM Microwave Imager. The Final Run product incorporates monthly gauge corrections and retrospective calibration, making it suitable for climate-scale analysis. Previous evaluations over the Indian region suggest that IMERG reasonably captures large-scale monsoon rainfall characteristics as well as sub-daily variability, supporting its application in studies of monsoon dynamics across multiple temporal scales (Murali Krishna et al., 2017; Ponukumati et al., 2023). However, some systematic biases in rainfall intensity and reduced accuracy during short-duration extreme events have been reported, particularly over complex terrain and at finer temporal scales. IMERG provides near-global coverage (90°S to 90°N) at high spatial resolution (0.1° × 0.1°) and a temporal resolution of 30 minutes, enabling robust assessment of precipitation variability from diurnal to seasonal time scales, which is particularly relevant for investigating multi-scale variability of the Indian summer monsoon.

2.2 Models

2.2.1 ICON

ICON model was developed through a joint initiative of the German Weather Service (DWD) and the Max Planck Institute for Meteorology (MPI-M) to provide a unified framework for numerical weather prediction and climate modelling (Zängl et al., 2015). ICON was explicitly designed to transition toward a fully non-hydrostatic dynamical core capable of resolving cloud-scale processes (Zängl et al., 2015; Wan et al., 2013). This non-hydrostatic core employs prognostic density and virtual potential temperature to ensure local mass conservation and uses a stable two-time-level predictor-corrector scheme that performs robustly over steep orography, an essential requirement for monsoon regions characterized by strong terrain-convection interactions. Very recently, ICON has also been adapted for exascale computing through GPU acceleration and domain-specific languages such as GT4Py, enabling multi-year global simulations at kilometer-scale resolution in experimental configurations (Lapillonne et al., 2026; Prein et al., 2026). The present set up uses ICON EXCLAIM version with a GT4Py dycore to run the experiments (Dipankar et al., 2026).

2.2.1.1 Model Configuration

The simulation was performed on the ALPS high-performance computing (HPC) infrastructure of the Swiss National Computing Center using 22 GPU nodes (NVIDIA GH200) for model integration and two dedicated nodes for input/output operations. A horizontal grid spacing of 40 km was used with 120 terrain-following vertical levels based on the smooth level vertical (SLEVE) coordinate (Leuenberger et al., 2010). The numerical time step for dynamics was 180s. Physical parameterizations were called at varying frequencies: convection, cloud cover, subgrid-scale orography, and non-orographic gravity wave drag schemes every 12 minutes, and radiation every 30 minutes.



2.2.1.2 Initial and Boundary Conditions

The simulation was initialized from European Center for Medium-Range Weather Forecasts (ECMWF) operational analysis on 1979-01-01 at 00:00 UTC, and run continuously until 2022-01-01 at 00:00 UTC. Sea surface temperature and sea ice cover were prescribed from the PCMDI AMIP II dataset (Taylor et al., 2000), updated monthly. The global aerosol climatology was provided by the Max-Planck-Institute Aerosol Climatology version 2 (MAC-v2) at 1° resolution (Kinne, 2019). Static surface fields (topography, land cover, vegetation, and soil properties) were prepared using the External Parameters for Numerical Weather Prediction and Climate Applications software (Asensio et al., 2020).

2.2.1.3 Physics Parameterizations

Deep and shallow convection were parameterized using the Tiedtke-Bechtold bulk mass flux scheme (Bechtold et al., 2001). Cloud microphysics followed a single-moment scheme for cloud water, cloud ice, snow, and rain (Hong and Lim, 2006). Land surface processes were simulated with the TERRA soil–vegetation–atmosphere transfer model (Schulz and Vogel, 2020) using eight soil levels. Turbulent transport in the boundary layer and surface exchange was represented using a turbulent kinetic energy-based scheme with a second-order closure (Raschendorfer et al., 2003).

2.2.2 CMIP6-AMIP

To provide a comprehensive intercomparison framework, we analyze atmospheric simulations from five CMIP6 models: CNRM-CM6-1-HR, MPI-ESM1.2-HR, GFDL-CM4, MIROC6, and the IITM-ESM. These models are selected based on the availability of sub-daily (3-hourly) temporal resolution, with higher spatial resolution used wherever available. All models are evaluated in their AMIP configuration, which prescribes observed sea surface temperatures and sea ice concentrations. The selected models span a range of horizontal resolutions (50–190 km), dynamical cores (hydrostatic spectral, finite-volume, and semi-Lagrangian formulations), and convection parameterization schemes (details provided in Table 1). For better understanding models having horizontal resolution less (more) than 100 km is considered as higher (coarser) resolution models.



Model	Organisation / Institute	Convective parametrisation	Microphysics	Spatial resolution (°)	Temporal resolution	Dynamical core	Reference
ICON	Max Planck Institute for Meteorology, Germany	Mass-flux schemes with shallow and deep convection (Tiedtke, 1989; Bechtold et al., 2008)	Single-moment scheme (Seifert, 2008)	0.4 × 0.4	1-hour	Non-hydrostatic; solved on a triangular icosahedral grid	(Müller et al., 2025; Dipankar et al., 2026)
CNRM-CM6-1-HR	Centre National de Recherches Météorologiques (CNRM), France	Prognostic treatment of dry, shallow, and deep convection (Piriou et al., 2007; GUÉRÉMY, 2011)	Convective microphysics by Bretherton et al. (2004) and Stratiform microphysics scheme by Lopez (2002)	0.5 × 0.5	3-hour	Hydrostatic; uses a two-level semi-Lagrangian numerical integration scheme	Voltaire (2019); Voltaire et al. (2019)
MPI-ESM1.2-HR	Max Planck Institute for Meteorology, Germany	Mass-flux scheme (ECHAM6.3) with tuned conversion rates and removal of CAPE	ECHAM6.3 microphysics with tuned ice fall velocity and Bergeron–Findeisen thresholds	0.9 × 0.9	3-hour	Hydrostatic; employs a spectral dynamical core with T127 truncation	Jungclaus et al. (2019); Müller et al. (2018)
GFDL-CM4	Geophysical Fluid Dynamics Laboratory, USA	New “double-plume” convective closure for shallow and deep convection	Aerosol and cloud microphysics modules similar to AM3 with modifications to indirect aerosol effects	1.25 × 1.0	3-hour	Hydrostatic version of the cube-sphere finite volume (FV3) dynamical core	Guo et al. (2018); Held et al. (2019)
MIROC6	JAMSTEC, Japan	Chikira and Sugiyama (2010) entrainment plume model and Park and Bretherton (2009) shallow convection	Standard cloud microphysics inherited from MIROC5	1.4 × 1.4	3-hour	Hydrostatic; uses a spectral dynamical core with T85 spectral truncation	Hajima et al. (2020); Tatebe et al. (2019)
IITM-ESM	Indian Institute of Tropical Meteorology (IITM), India	Revised Simplified Arakawa-Schubert (SAS) convection scheme (Han and Pan, 2011)	Zhao-Carr scheme (Zhao and Carr, 1997)	1.8 × 1.9	3-hour	Hydrostatic; spectral general circulation model with T62 triangular truncation	Narayanasetti et al. (2020); Krishnan et al. (2019)

Table 1. Description of models used in this study



2.3 Methodology

170 2.3.1 Harmonic Analysis

The fundamental form of the harmonic equation used in this analysis is expressed in the combined sine–cosine form:

$$P = \bar{P} + \sum_{i=1}^{n/2} \left[a_i \cos\left(\frac{2\pi it}{T}\right) + b_i \sin\left(\frac{2\pi it}{T}\right) \right] \quad (2)$$

where P represents the precipitation data (ICON, CNRM, MPI, GFDL, MIROC, IITM-ESM and IMERG), and \bar{P} denotes the mean value of n observations. The subscript i indicates the harmonic number, corresponding to the first, second, up to the 175 n^{th} harmonics of the period T (for diurnal analysis, $T = 24$ hours). The variable t represents time in hours (for IMERG data: 0000, 0030, 0100, ..., 2300, 2330).

The maximum number of harmonics that can represent the full series is $n/2$. For example, half-hourly GPM-IMERG data, consisting of 48 observations within one period T , can be represented by 24 harmonics. Similarly, ICON datasets with 1-hourly time steps (24 observations) can be represented by 12 harmonics, while other models with 3-hourly time steps (8 observations) 180 can be represented by 4 harmonics.

The first ($i = 1$) and second ($i = 2$) harmonics represent the diurnal (24-hour) and semi-diurnal (12-hour) variability, respectively. The coefficients a_i and b_i correspond to the coefficients of the cosine and sine components of each harmonic, respectively. The amplitude (A_i) and phase (Φ_i) are defined as:

$$A_i = \sqrt{a_i^2 + b_i^2} \quad (3)$$

$$185 \quad \Phi_i = \tan^{-1}\left(\frac{b_i}{a_i}\right) \quad (4)$$

Here, A_i represents the diurnal amplitude (the magnitude of maximum rainfall variation), and Φ_i denotes the phase (the timing of the maximum rainfall) for the i^{th} harmonic.

2.3.2 Empirical orthogonal function analysis

To examine the dominant spatial structures of diurnal rainfall variability, Empirical Orthogonal Function (EOF) analysis 190 (Lorenz, 1956) is applied to rainfall anomalies obtained by removing the daily mean at each grid point. The analysis is performed over the domain shown in Fig. 2. The leading EOF modes represent coherent patterns of the diurnal cycle, including stationary responses over land and propagating signals associated with coastal and orographic convection. Model fidelity is evaluated by comparing the spatial structure and explained variance of these modes with IMERG observations.

In EOF analysis, the spatial eigenvectors represent the dominant spatial patterns of variability, while the associated principal 195 components (PCs) describe their temporal evolution. Such a decomposition allows the separation of spatial structures



and temporal variability of rainfall, facilitating the identification of distinct diurnal regimes. Model performance can further be assessed by comparing the temporal correlation of PCs and the spatial errors of EOF patterns between observations and simulations (Huang and Wang, 2017).

3 Results and Discussion

200 3.1 Assessment of diurnal scale variability in models with observation

The diurnal cycle of precipitation provides a stringent benchmark for evaluating model fidelity, as it reflects the coupled evolution of boundary-layer thermodynamics, convective triggering, cloud–radiative feedback, and mesoscale organization (Johnson, 2011). Over the Indian monsoon region, the diurnal signal is strongly modulated by orography, land–sea thermal contrasts, and the background monsoon circulation (Sahany et al., 2010). Accurate simulation of both the amplitude and phase
205 of the diurnal harmonic is therefore essential to check how models simulate convective processes across heterogeneous terrain and adjacent oceanic regions.

3.1.1 Diurnal Amplitude and Phase

The climatological mean diurnal amplitude of rainfall during the Indian summer monsoon for June, July, August, September (JJAS) period for 1979–2014 from ICON and five CMIP6 models (CNRM, MPI, GFDL, MIROC, and IITM-ESM) is evaluated
210 against IMERG (Fig 1). ICON skilfully simulates the large-scale spatial distribution of the observed diurnal amplitude over the Indian landmass and adjoining oceans (Fig 1a, g), but with systematic overestimation along the Himalayan foothills, the Arakan Yoma range, and the Western Ghats. Over the eastern equatorial Indian Ocean, particularly within the Oceanic Tropical Convergence Zone (OTCZ), ICON simulates nearly double the observed diurnal amplitude, indicating enhanced diurnal modulation of oceanic convection.

215 Among CMIP6 high-resolution models, CNRM reasonably reproduces the spatial pattern of diurnal amplitude but underestimates its magnitude, especially over CI and the equatorial Indian Ocean (Fig 1b). MPI shows pervasive overestimation across the entire domain (Fig 1c), characterized by unrealistic wave-like artifacts. Coarser-resolution models such as GFDL (Fig 1d), MIROC (Fig 1e), and IITM-ESM (Fig 1f) fail to adequately resolve the smaller topographic features resulting in diurnal maxima along the Western and Eastern Ghats, appear fragmented rather than forming continuous bands as seen in IMERG. Such
220 fragmentation and reduced intensity over complex terrain are consistent with earlier findings that coarse horizontal resolution and parameterized convection can smooth sharp precipitation gradients and weaken orographic rainfall contrasts (e.g. Basu, 2007; Krishnamurti et al., 2007, etc.). Despite their coarser resolution, GFDL and MIROC capture the broad spatial pattern of diurnal amplitude. GFDL displays a southwestward shift of the BoB maximum, whereas the characteristic diurnal maximum over the northern Gangetic plains is largely absent in IITM-ESM.

225 The RMSE, pattern correlation (PCC) summary (Fig. 1h), computed over the study domain shown in the Fig. 1a-g, highlights a trade-off between spatial fidelity and magnitude bias. ICON shows the highest PCC (~ 0.8) but relatively larger RMSE (~ 2.7

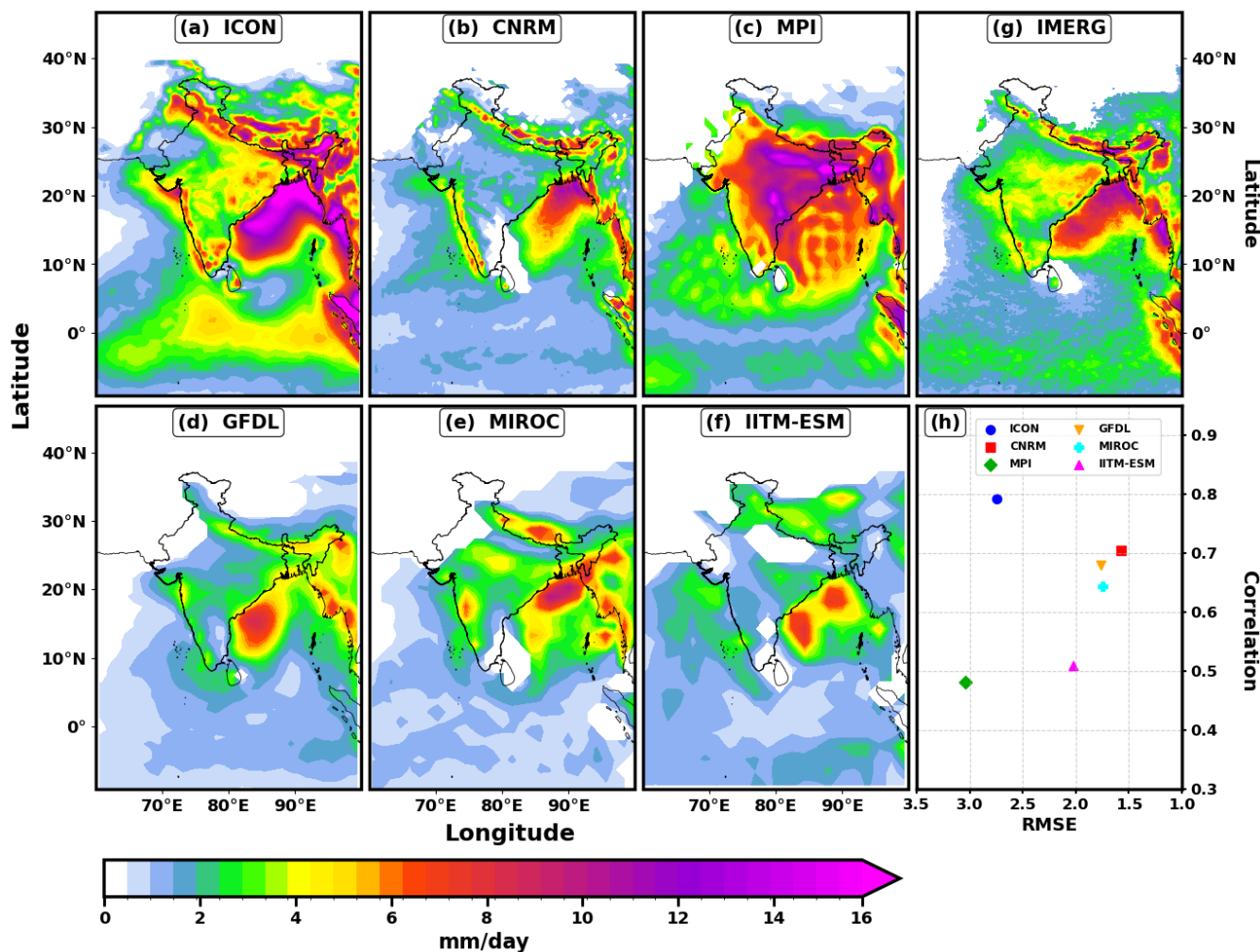


Figure 1. Climatological mean diurnal amplitude of precipitation (mm day^{-1}) during the Indian summer monsoon season (JJAS) from (a-f) ICON, CNRM, MPI, GFDL, MIROC, and IITM-ESM model simulations, with (g) IMERG as the observational reference. Panel (h) shows the relationship between model performance metrics, with a scatterplot of pattern correlation versus root-mean-square error (RMSE) for all models relative to IMERG.

230 mm day^{-1}), reflecting amplitude overestimation. CNRM, GFDL, and MIROC exhibit moderate correlation (~ 0.6 – 0.7) with lower RMSE (1.5 – 1.8 mm day^{-1}), while MPI and IITM-ESM show weaker correlation (~ 0.5). IITM-ESM, despite its coarser resolution, maintains lower RMSE ($\sim 2.0 \text{ mm day}^{-1}$) than ICON due to systematic amplitude underestimation. These results indicate that improved spatial agreement does not necessarily correspond to reduced mean error, and that amplitude bias exerts a dominant influence on RMSE across models.

The spatial pattern of diurnal rainfall bias highlights regionally organized systematic errors and provides additional context to the diurnal amplitude structure. ICON exhibits relatively modest bias over most continental regions but shows pronounced



positive bias over oceanic convective zones and along the Himalayan foothills (Fig 2a). Notably, these regions are characterized by late-night to early-morning diurnal maxima in observations. The systematic overestimation in these areas suggests difficulties in representing convection that peaks during nocturnal or early-morning hours, when boundary-layer thermodynamics and large-scale dynamical forcing differ substantially from daytime conditions. Further, in ICON simulations the positive bias over the northern BoB is amplified. This region is known for strong diurnal propagation and organized mesoscale convection (e.g. Johnson, 2011; Fujinami et al., 2005) and misrepresentation of these physical processes likely contributes to the enhanced amplitude bias in ICON. Among the CMIP6 models, MPI exhibits the most pronounced overestimation of diurnal amplitude across nearly the entire domain, with only localized underestimation over parts of the northern and western BoB (Fig 2c). In contrast, CNRM, GFDL, MIROC, and IITM-ESM predominantly underestimate diurnal amplitude over both land and ocean, indicating a systematic negative bias across much of the monsoon region.

Regional means are calculated over the CI land region (16.5–26.5°N, 74.5–86.5°E; Goswami et al., 2006) and the BoB ocean region (12–22.5°N, 80–99°E; Pokhrel et al., 2018b), as shown in Fig 2f, further quantify these contrasts in Table 2. ICON shows a modest positive bias over CI (+0.36 mm day⁻¹) but a substantially larger bias over the BoB (+3.91 mm day⁻¹), highlighting a pronounced land–ocean contrast. Except for MPI, which exhibits strong positive bias over land (+6.16 mm day⁻¹), all CMIP6 models show negative bias over both regions (-0.71 to -2.54 mm day⁻¹). IITM-ESM exhibits -2.23 mm day⁻¹ over CI and -2.54 mm day⁻¹ over the BoB, reflecting a muted diurnal amplitude across both land and ocean.

Models	CI	BoB
ICON	0.36	3.91
CNRM	-2.00	-1.32
MPI	6.16	0.66
GFDL	-1.52	-1.63
MIROC	-0.71	-1.54
IITM	-2.23	-2.54

Table 2. Mean diurnal rainfall bias (mm day⁻¹) averaged over the Central India (CI) and Bay of Bengal (BoB) boxes, as defined in Fig 2f.

The normalized evening (1200–2300 LT) minus morning (0000–1100 LT) rainfall highlights the canonical land–ocean phase contrast of the monsoon region (Fig 3). In IMERG (Fig 3g), most of the Indian landmass exhibits a dominant afternoon–evening maximum, whereas adjacent oceanic regions show prevailing morning rainfall, consistent with earlier satellite analyses (Johnson, 2011). Two notable exceptions emerge: (i) the Himalayan foothills, where rainfall peaks during late night to early morning due to nocturnal low-level convergence and orographic effects (Barros and Lang, 2003; Fujinami et al., 2005; Chen, 2020), and (ii) the central BoB, where an afternoon maximum replaces the typical oceanic morning peak, associated with westward-propagating mesoscale convective systems (MCSs) and gravity-wave modulation (Johnson, 2011).

ICON reproduces the large-scale land–ocean contrast and the key exception regions with relatively high spatial agreement (PCC = 0.79; Fig 3a). However, the Himalayan morning maximum is displaced southward and an additional morning signal emerges along the eastern Indian coast, leading to a substantial CI phase-related amplitude bias (-2.5 mm day⁻¹). This trade-

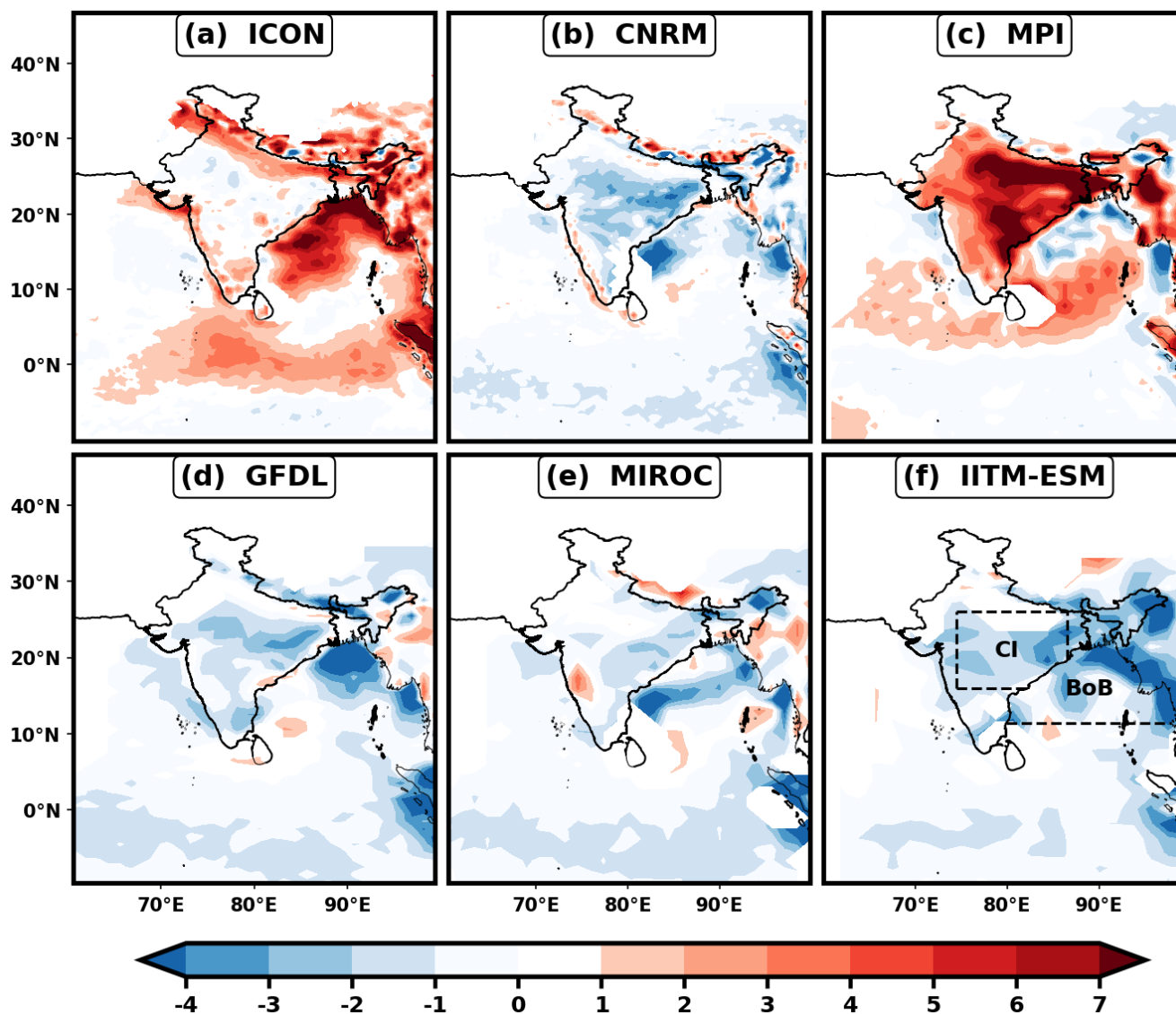


Figure 2. Spatial distribution of JJAS climatological mean diurnal precipitation amplitude bias (mm day^{-1}) relative to IMERG for (a-f) ICON, CNRM, MPI, GFDL, MIROC and IITM-ESM. The two representative regions Central India (CI), and the Bay of Bengal (BoB) used for regional bias analysis (Table 2) are indicated in panel (f). The boxes are bounded by land boundaries and dashed outlines such that CI excludes oceanic grid points and BoB excludes land grid points.



260 off between spatial correlation and regional bias is evident in the CI bias–PCC scatter plot (Fig 3h). Among the CMIP6 models, CNRM shows a comparable magnitude of CI bias despite lower pattern correlation (0.6). In contrast, MPI despite deficiencies in representing regional phase reversals as indicated by the lowest PCC (0.2), it exhibits a smaller CI bias (-0.8 mm day^{-1}), followed by MIROC (-0.2 mm day^{-1}), indicating that reduced structural fidelity does not necessarily imply larger regional amplitude error. Among the remaining models, GFDL and IITM-ESM show very weak diurnal contrast, with limited skill in
265 reproducing the continental timing, as indicated by lower PCC and higher CI bias. IITM-ESM additionally exhibits a southward shift of the BoB signal and an unrealistic evening dominance over parts of the Arabian Sea. MIROC performs comparatively better among the coarser models, capturing the primary contrast and regional phase behaviour, though with reduced intensity. Overall, inter-model differences primarily reflect their ability to capture regional phase reversals and the sharp land–ocean transition, which are critical characteristics of the monsoon diurnal cycle. The subsequent discussion on the spatial phase
270 biases will make it more clear.

To complement the spatial diagnostics, the composite diurnal cycle over CI and the BoB is examined (Fig S1). ICON reproduces the observed diurnal cycle over CI with realistic amplitude and minimal phase error, whereas most CMIP6 models exhibit reduced amplitudes and earlier peaks, with MPI showing a pronounced overestimation of amplitude and an unrealistic early peak. Over the BoB, ICON overestimates the diurnal amplitude but captures the phase more accurately than other models,
275 which generally display weaker amplitudes and delayed peaks. The amplitude–phase error characteristics further confirm that ICON performs comparatively better in phase representation across both regions, despite residual amplitude biases, particularly over the ocean. These regional characteristics are further reflected in the spatial distribution of phase biases discussed below.

The diurnal phase of precipitation over the Indian subcontinent remains a significant challenge for state-of-the-art climate models, with both ICON and CMIP6 models exhibiting pervasive systematic biases in rainfall timing (Fig 4a-f). Over most
280 of the Indian landmass, models tend to produce rainfall prematurely, with an early bias upto 9 hours. ICON (Fig 4a) shows the smallest early bias, whereas MPI (Fig 4c) exhibits the largest. Along the Himalayan foothills, ICON displays a delayed phase, particularly over the western Gangetaic basin, a feature absent in other models. The relatively reduced early bias in ICON and CNRM suggests some sensitivity to horizontal resolution, while coarser models such as GFDL and MIROC display widespread premature initiation. IITM-ESM, despite its coarse resolution, shows comparatively weaker early bias over parts
285 of CI. Premature convection over land has been widely attributed to deficiencies in convective parameterization schemes, which trigger rainfall near local noon rather than the observed late-afternoon peak (Jha et al., 2022; Sahany, 2009). This early triggering limits the buildup of CAPE, leading to weakened and temporally displaced rainfall maxima (Hunt et al., 2022; Krishnamurti et al., 2007; Krishna et al., 2021). Over the surrounding oceans, models generally exhibit a late phase bias of up to 12 hours, consistent with excessive persistence of stratiform precipitation (Pokhrel and Sikka, 2013). The BoB differs from
290 this general oceanic behaviour, with most models producing rainfall too early. ICON shows an average 3-hour early bias over the BoB, increasing to 6 hours in MPI and GFDL, while MIROC and IITM-ESM display smaller, spatially confined early biases.

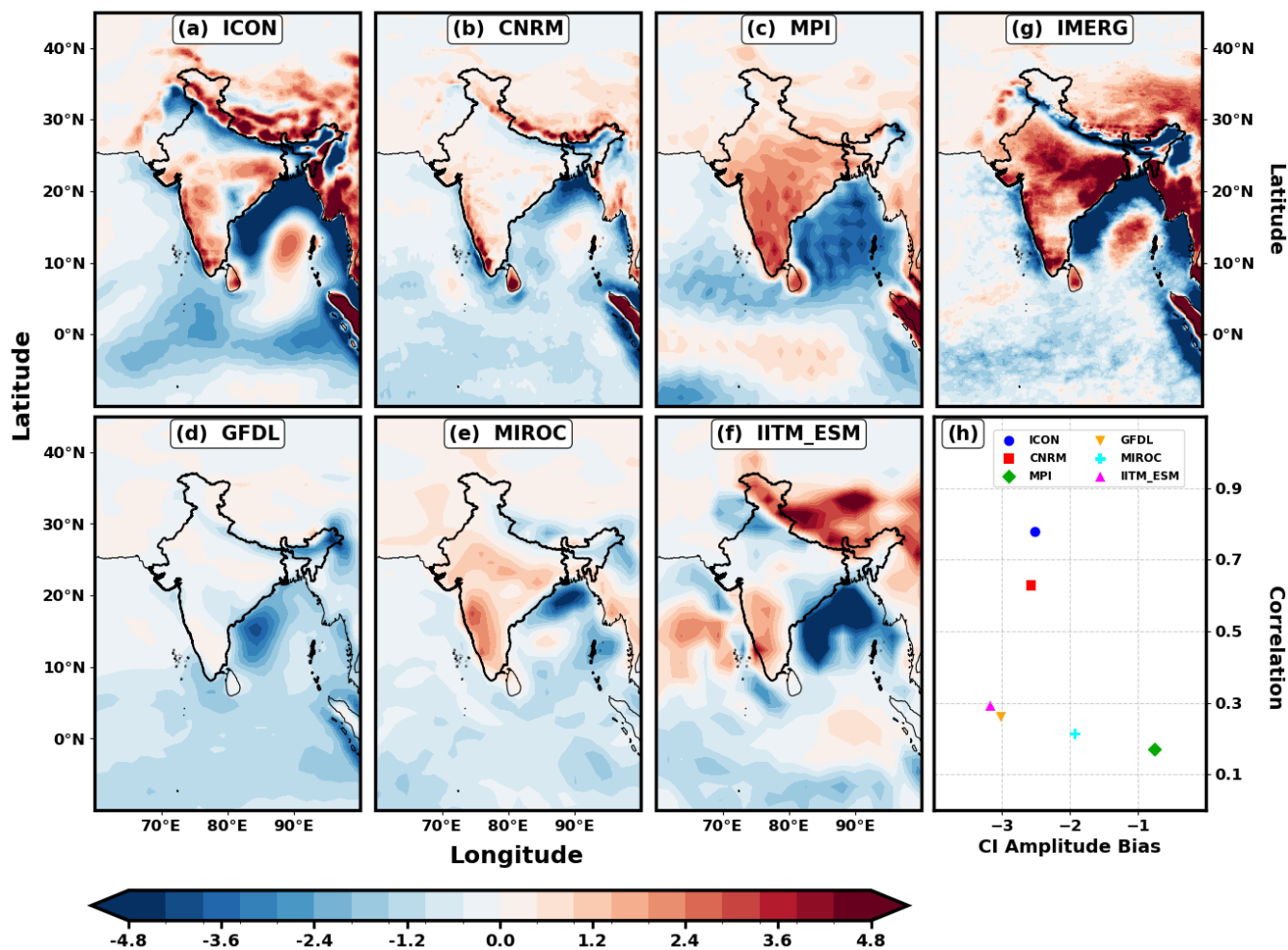


Figure 3. Climatological mean JJAS evening (1200–2330 LT) minus morning (0000–1130 LT) precipitation for the period 1979–2014, normalized by the JJAS mean rainfall, derived from (a-f) ICON, CNRM, MPI, GFDL, MIROC, and IITM-ESM model simulations. Panel (g) shows IMERG observations, while panel (h) shows the pattern correlation of each model with IMERG and the Central India (CI) mean amplitude difference between models and IMERG (Model-IMERG). Precipitation is expressed in mm day^{-1} .

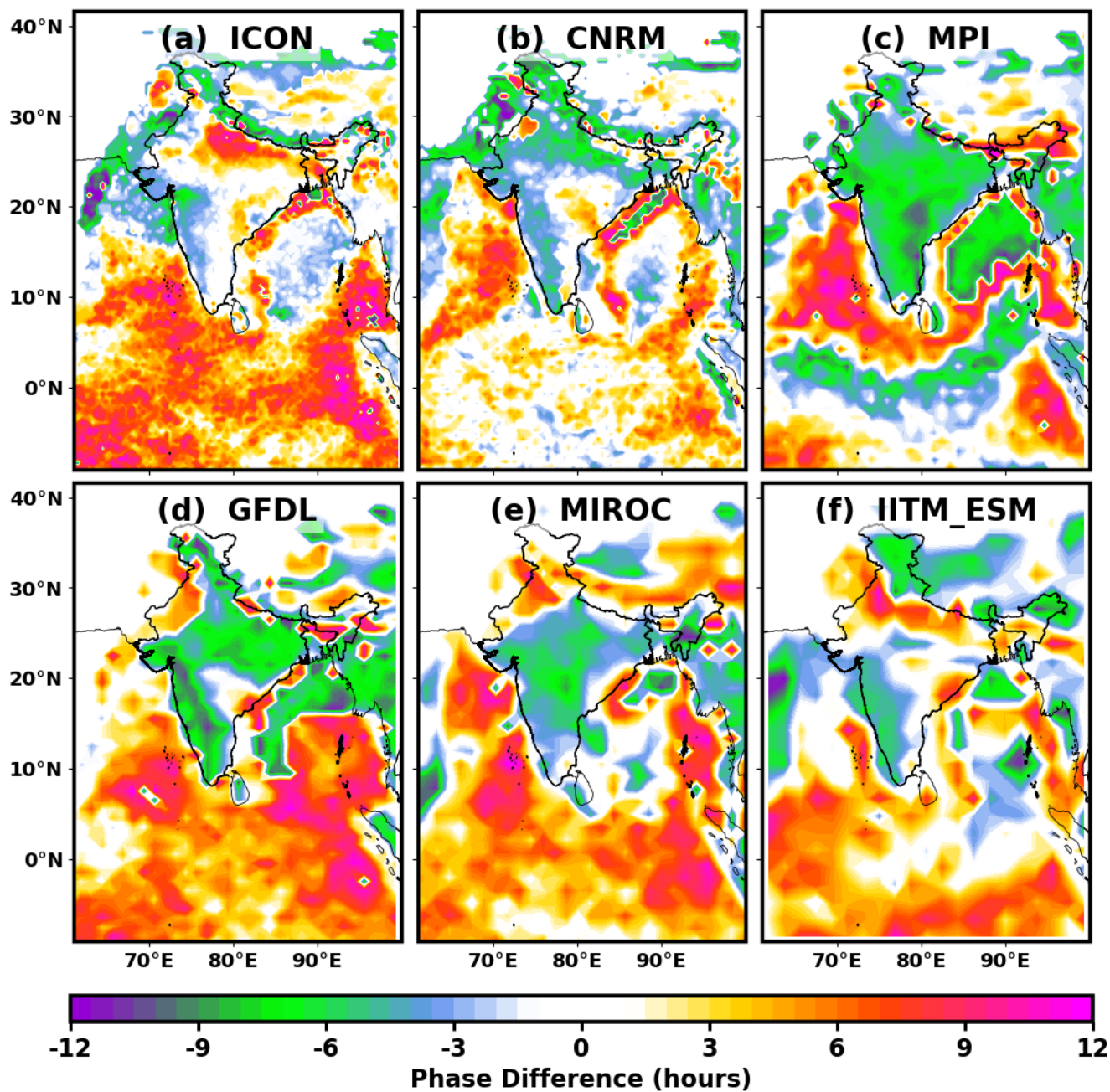


Figure 4. Climatological mean JJAS diurnal phase bias of precipitation (in hours) relative to IMERG from (a-f) ICON, CNRM, MPI, GFDL, MIROC, and IITM-ESM model simulations.



The combined amplitude and phase analyses demonstrate that while ICON substantially improves the timing and intensity of diurnal rainfall compared to CMIP6 models, notable regional discrepancies persist, particularly over complex terrain and oceanic convection zones. To further examine the spatiotemporal structure of the diurnal signal, an EOF analysis is employed.

3.1.2 EOF analysis of diurnal rainfall

To identify dominant patterns of diurnal rainfall variability, we apply EOF analysis, which efficiently reduces the dimensionality of large datasets while retaining the key physical modes (Hannachi et al., 2007). EOFs are widely used in diurnal cycle studies as they capture coherent spatial–temporal structures that explain most of the observed variance. In high-resolution satellite data, the first two EOF modes typically account for over 80–90% of the total variance (Lee and Wang, 2021). Higher-order modes generally correspond to semidiurnal oscillations (Kikuchi and Wang, 2008) and are not discussed here. Hence, our analysis focuses on the first two EOF modes to evaluate the ability of ICON and CMIP6 models to reproduce the principal diurnal rainfall regimes over the Indian monsoon region.

3.1.2.1 EOF1

The first EOF spatial mode (EOF1) in IMERG exhibits a pronounced land–ocean contrast, with positive loadings over most of the Indian landmass and negative loadings over adjacent oceanic regions, apart from a few regional exceptions (Fig 5g). This bipolar structure represents the spatial signature of the diurnal harmonic and reflects differential surface heating arising from contrasting land–sea heat capacities. Such a land–sea contrast pattern is a robust feature of the atmospheric response to daily radiative forcing and has been consistently documented in earlier studies (Kikuchi and Wang, 2008; Lee and Wang, 2021). EOF1 explains approximately 64% of the total variance, confirming its dominance in diurnal precipitation variability. Enhanced loadings along coastlines and elevated terrain—including the Himalayas, Western Ghats, and Arakan Yoma—indicate intensified diurnal convection linked to localized sea-breeze and valley-breeze convergence. The negative loadings over parts of the Himalayas reflect the nocturnal to early-morning rainfall peak (0000–0600 LST), nearly 12 hours out of phase with the afternoon maximum over most of the Indian landmass.

The ICON model closely reproduces the observed EOF1 land–ocean contrast pattern (Fig 5a), including the key regional features seen in IMERG (Fig 5h), though with slightly weaker intensity over land. The negative loadings along the Himalayas appear broader and exhibit a modest southward displacement, and an additional weak negative center emerges along the eastern coastal landmass, which is absent in the IMERG pattern. Overall, ICON’s EOF1 accounts for 59% of the total variance, approximately 5% lower than IMERG, indicating a comparable but slightly weaker representation of the dominant diurnal mode. Among the CMIP6 models, several capture aspects of the land–sea contrast with varying fidelity. The high-resolution CNRM model most closely matches IMERG, both spatially and in variance explained (62%), although the amplitude of loadings is substantially reduced (Fig 5b). MPI model produces a stronger-than-observed bipolar contrast (Fig 5c), explaining nearly 75% of the variance around 9% higher than IMERG. Despite its coarser resolution, MIROC realistically captures the spatial structure of the EOF1 mode (Fig 5g), though with reduced variance (54%). In contrast, GFDL and IITM-ESM fail to reproduce

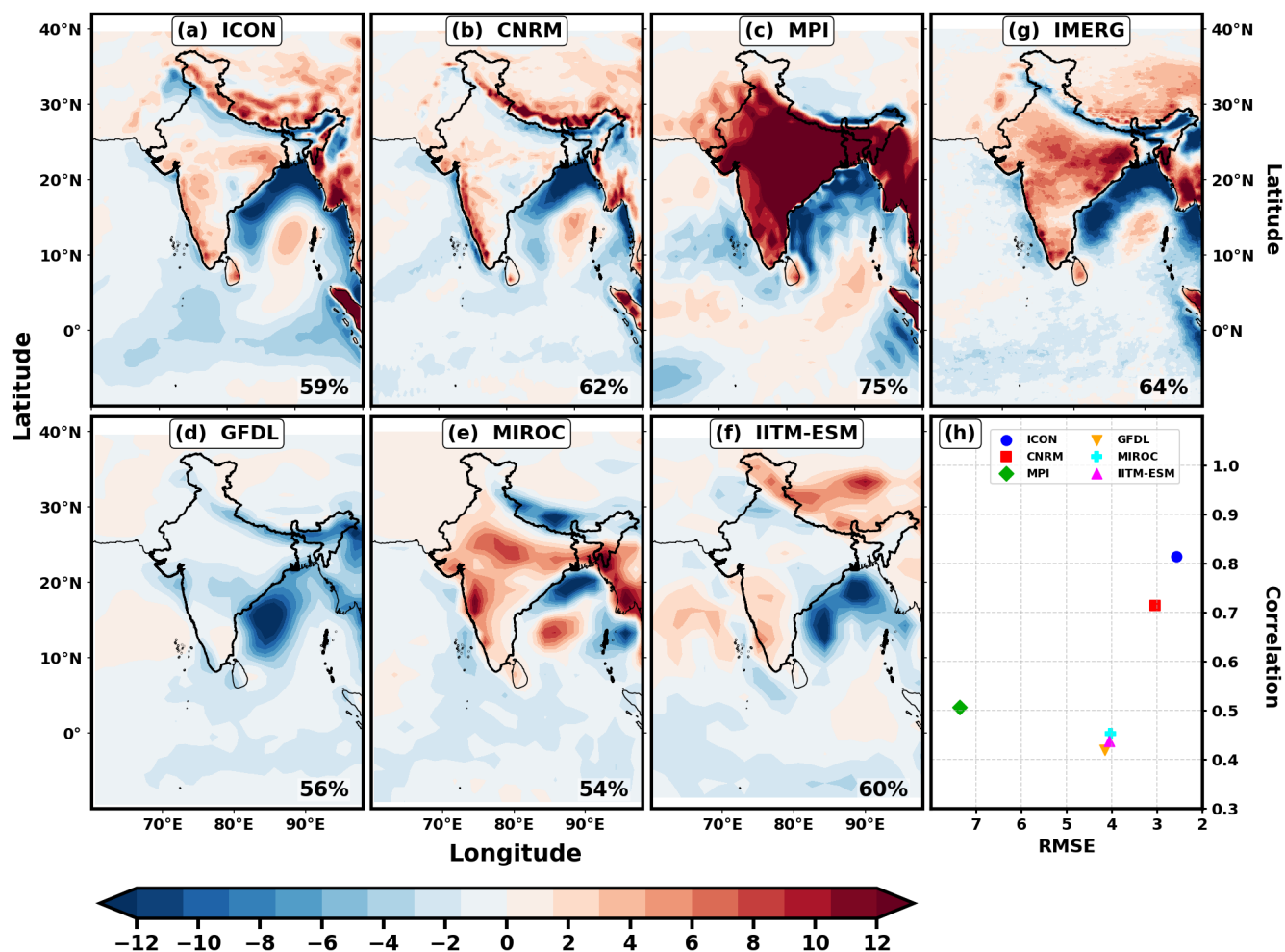


Figure 5. Spatial loading patterns of EOF1 for JJAS diurnal rainfall from (a-f) ICON, CNRM, MPI, GFDL, MIROC, and IITM-ESM model simulations, with (g) IMERG as the observational reference. Panel (h) shows the relationship between the spatial pattern correlation of EOF1 and the RMSE. The number in the lower right corner of each panel denotes the percentage of total variance explained by EOF1.

325 the characteristic land–ocean structure: GFDL exhibits predominantly negative loadings with weak contrast (Fig 5d), while IITM-ESM shows widespread negative loadings over land and only weak positive signals over the peninsula.

The comparative performance of these models is further quantified using the pattern correlation coefficient (PCC) and root-mean-square error (RMSE) of the EOF1 spatial distribution relative to IMERG. ICON shows the highest pattern correlation (PCC = 0.83) and lowest RMSE (2.3), followed by CNRM (PCC ≈ 0.7). GFDL, MIROC, and IITM-ESM exhibit comparable skill (PCC ≈ 0.42; RMSE ≈ 4.0). The MPI model, despite its strong spatial contrast, shows the largest RMSE (7) among all models, reflecting its tendency to overamplify the land–ocean gradient.

330



3.1.2.2 EOF2

The second EOF mode (EOF2) of diurnal precipitation is often termed as the Transition or the Coastal Mode. It represents the geographical variations that deviate from the universal land–sea contrast as captured by EOF1. While EOF1 explains the direct thermodynamic response to solar forcing, EOF2 classifies the complex diurnal regimes, associated with coastal propagation and topographic influences, including the relative strength of nighttime convection and phase propagation over complex terrain (Kikuchi and Wang, 2008).

In IMERG, EOF2 mode (Fig 6g) displays distinct zonal and meridional gradients on either side of major coastal and orographic features and explains 27% of the total variance. Positive loadings appear along the northern BoB and adjoining eastern coastal regions (northern Andhra Pradesh, Odisha, and West Bengal), while negative loadings dominate the southern Bay and southern east coast (southern Andhra Pradesh and Tamil Nadu). Over the Himalayan foothills, contrasting loadings emerge, with negative anomalies over the mountains and positive anomalies immediately southward, consistent with enhanced nocturnal convection in the plains and suppressed activity over elevated terrain. The peninsular interior is characterized largely by negative loadings. Among the models, the representation of this mode shows considerable diversity, reflecting the difficulty in simulating coastal and orographically triggered diurnal convection. The high-resolution models ICON and CNRM reproduce the broad spatial structure, but with some regional differences. ICON provides the closest match to IMERG, explaining 25% of the total variance, while successfully capturing the alternating loadings along the eastern coastline. However, it reverses the sign of loadings over the Himalayas. CNRM similarly reproduces the eastern coastal features but fails to represent the Himalayan pattern. Among the coarser models, MIROC depicts the coastal–inland gradients reasonably well, while MPI shows partial agreement but with spatial artifacts. GFDL and IITM-ESM display distorted and weak loading structures, indicating limited fidelity. In terms of explained variance, GFDL (39%), MIROC (35%), and CNRM (31%) overestimate the contribution of EOF2, whereas IITM-ESM (22%) and MPI (17%) underestimate it. Pattern statistics further distinguish model performance hierarchy with, ICON leading with highest correlation ($PCC \approx 0.6$) and lowest RMSE ($\sim 2.5 \text{ mm day}^{-1}$), followed by CNRM ($PCC \approx 0.5$; $RMSE \approx 2.8 \text{ mm day}^{-1}$). MIROC and MPI show moderate correlation ($PCC \approx 0.4$), though MPI retains larger error. GFDL exhibits negative correlation and the highest RMSE, indicating poor representation of this mode, while IITM-ESM, despite low PCC (~ 0.2), captures some aspects of the propagating structure.

The spatial structure captured by EOF2 underscores the strong influence of coastal and orographic processes on the diurnal organization of rainfall, particularly between the eastern coastline and the BoB. However, the spatial loadings alone do not fully resolve the temporal evolution and migration characteristics embedded within this mode. To examine whether EOF2 represents organized eastward or coastal-propagating convection, a lead–lag regression analysis based on the EOF2 principal component (PC) is conducted in the following section.

To examine the propagation characteristics of diurnal convection, PC2 is regressed against diurnal rainfall anomalies with a ± 15 -hour lead–lag over the latitudinal band 8°N – 16°N , corresponding to the region of eastward-propagating convective systems from the Indian landmass into the BoB, as indicated by the EOF2 spatial pattern. In IMERG (Fig 7g), a clear eastward propagation is evident. Positive anomalies appear near 80°E at lag -12 h and progressively shift eastward toward $\sim 90^\circ\text{E}$ by lag $+5 \text{ h}$, indicating a coherent propagating signal with an estimated phase speed of $\sim 16 \text{ ms}^{-1}$. The timing reflects afternoon

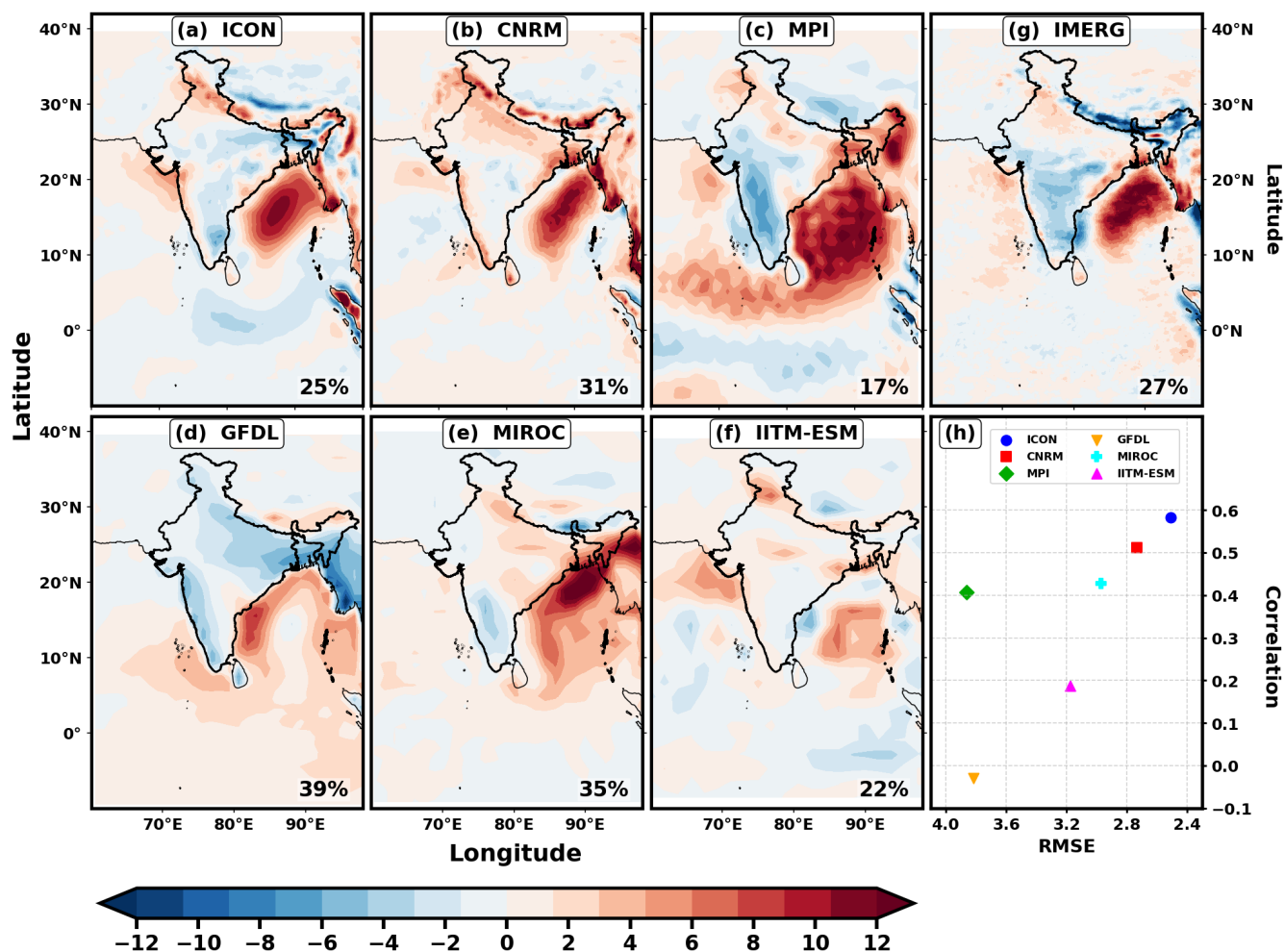


Figure 6. Same as Fig 5, but for EOF2.

convection over land followed by nighttime enhancement over the adjacent ocean, consistent with coastal propagation linked to land–sea-breeze circulations and mesoscale organization over the BoB (Kikuchi and Wang, 2008; Johnson, 2011). Such propagation is understood to arise from a combination of cold-pool–driven density currents, diurnally generated gravity waves, and land–sea thermal contrasts that modulate low-level convergence (Mapes et al., 2003; Yang and Slingo, 2001). Observational studies indicate that these signals typically travel at 8–15 ms^{-1} over open ocean—faster than over land due to reduced surface drag—and can persist for several hundred kilometers, with the organized rainfall episode lasting longer than individual convective cells (Johnson, 2011).

ICON (Fig 7a) reproduces the eastward-sloping regression structure and maintains a coherent propagating signal, though with slightly weaker amplitude and marginally faster phase speed than observed. CNRM captures the general eastward tilt but with reduced regression strength, indicating weaker coherence. In contrast, MPI, MIROC, and GFDL primarily exhibit



standing or weakly evolving structures with limited longitudinal progression, while IITM-ESM shows low regression amplitude and poorly organized propagation. The relative regression magnitudes (Fig 7h) further summarize these differences. IMERG exhibits the strongest signal (≈ 20), followed by ICON (≈ 15). Although MPI shows comparable amplitude, its pattern lacks clear propagation and is dominated by stationary features. The remaining models display weaker regression coefficients and limited temporal evolution, indicating difficulty in representing the propagating component of the diurnal cycle.

Overall, the lead-lag analysis demonstrates that simulating coastal diurnal propagation requires not only realistic amplitude but also coherent phase progression linked to mesoscale dynamics and land-ocean coupling processes. Differences across models suggest varying abilities to represent these interacting mechanisms

The comprehensive diurnal-scale assessment indicates that, although several models capture aspects of convective timing, amplitude, and coastal propagation, systematic biases remain particularly over complex terrain and along land-sea transition zones. Errors in phase, amplitude, and mesoscale propagation at the diurnal scale are not isolated deficiencies; they can influence how convection organizes, aggregates, and interacts with larger-scale circulation. This multiscale interaction is corroborated by recent observational evidence demonstrating that the diurnal amplitude of precipitation is actively amplified or suppressed during the wet and dry spells of high- and low-frequency ISOs, respectively (Misra and Jayasankar, 2026). Such biases may subsequently affect the representation of synoptic disturbances, ISOs, and ultimately the seasonal mean monsoon rainfall. To evaluate whether these scale-dependent errors persist or amplify across temporal hierarchies, the following sections examine model performance at synoptic (3–7 days), intraseasonal (10–90 days), and seasonal (>90 days) timescales.

3.2 Monsoon variability in other scales (Synoptic, intraseasonal, and seasonal)

3.2.1 Power Spectrum

The power spectral density (PSD) of daily rainfall quantifies the distribution of variance across temporal frequencies and provides insight into the temporal organization of monsoon convection (Torrence and Compo, 1998; Wheeler and Kiladis, 1999). Over CI, the IMERG spectrum (Fig 8g) exhibits well-defined peaks in three characteristic bands: synoptic disturbances (2–7 days), higher-frequency intraseasonal variability (10–20 days), and lower-frequency ISOs (30–60 days), consistent with established characterizations of monsoon variability (Goswami et al., 2006; Saha et al., 2014). The dominant peak occurs near 5.3 days with maximum power of $\sim 18 \text{ mm}^2 \text{ day}^{-2}$ (Fig 8h), and the spectrum displays the expected red-noise decay toward higher frequencies.

ICON (Fig 8a) reproduces the overall spectral shape and retains a dominant synoptic-scale peak at 7.6 days, though with reduced amplitude ($\sim 12\text{--}13 \text{ mm}^2 \text{ day}^{-2}$). A secondary signal appears in the 10–20-day band, marginally above the red-noise background, while the 30–60-day band is substantially underestimated. Thus, although the hierarchical structure of variability is maintained, intraseasonal power remains weakened. CNRM (Fig 8b) shifts its dominant peak toward the 10–20-day band (~ 9.4 days), producing one of the higher peak amplitudes among the models ($\sim 14 \text{ mm}^2 \text{ day}^{-2}$), but with comparatively weak synoptic and lower frequency intraseasonal variance. MPI (Fig 8c) exhibits the lowest overall spectral energy—approximately one-third of IMERG—with its maximum centered ~ 7.2 days ($\sim 6 \text{ mm}^2 \text{ day}^{-2}$), indicating muted variability across all timescales.

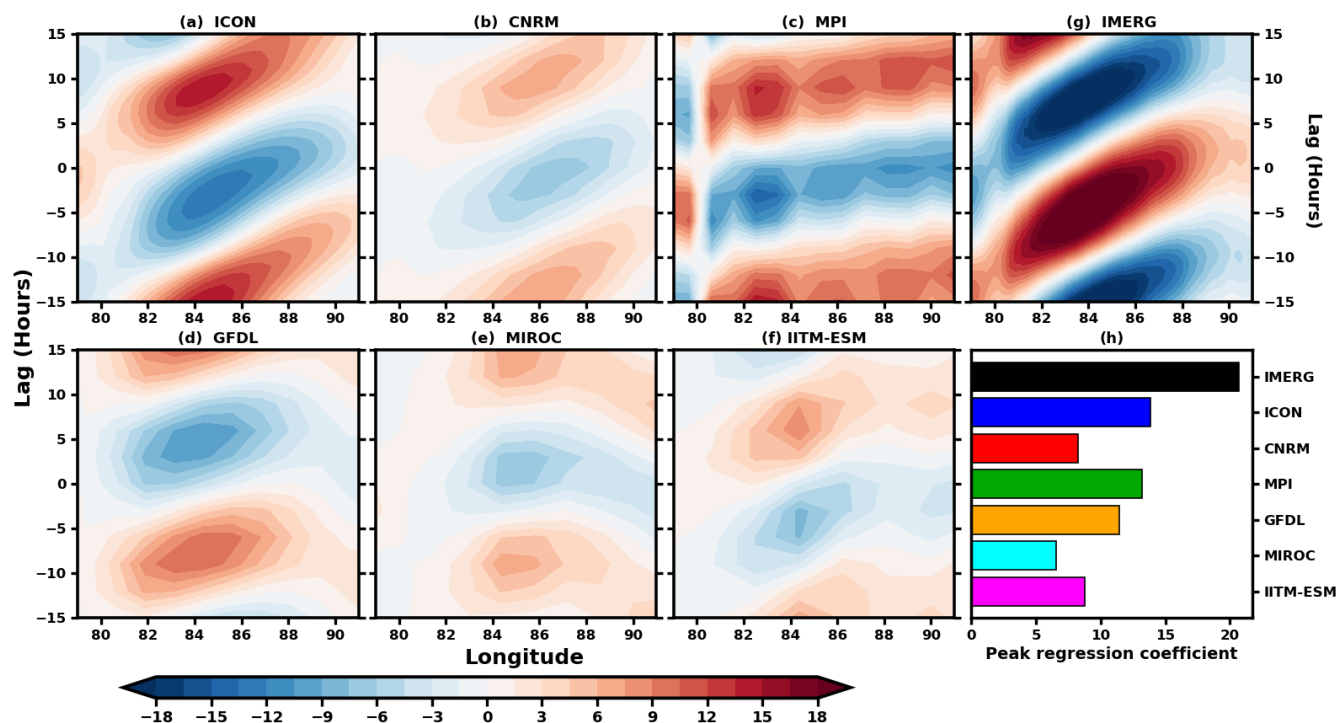


Figure 7. Eastward propagation of diurnal convective systems inferred from lead–lag regression (–15 to +15 h) between EOF2 principal component (PC2) and diurnal rainfall anomalies averaged over 8°–16°N. Results are shown for (a–f) ICON, CNRM, MPI, GFDL, MIROC, and IITM-ESM, with (g) IMERG as the observational reference. Panel (h) summarizes the peak regression coefficients for IMERG and all models.

410 Among the coarser-resolution models, MIROC (Fig 8e) most closely matches the observed dominant period (5.5 days) and produces a reasonable peak amplitude ($\sim 14 \text{ mm}^2 \text{ day}^{-2}$), though intraseasonal power remains underestimated. GFDL (Fig 8d) retains synoptic-band dominance (~ 8.1 days) but with weaker amplitude. In contrast, IITM-ESM (Fig 8f) shifts its primary peak into the 10–20-day band (~ 15.3 days), with moderate amplitude but limited synoptic-scale variance.

A consistent feature across all simulations is the marked underestimation of lower frequency intraseasonal (30–60-day) variability. Such weakening is commonly reported in AMIP-type integrations, where prescribed monthly SSTs limit two-way ocean–atmosphere feedbacks that are essential for sustaining coupled ISOs (Waliser et al., 2003; Jiang et al., 2020). Reduced synoptic-band power in several models further suggests limited representation of organized MCSs, which contribute substantially to rainfall variance at these periods. Overall, while several models reproduce the broad spectral hierarchy of monsoon rainfall, systematic reductions in variance—particularly in the intraseasonal bands—remain evident. These scale-
420 dependent differences in spectral power provide a dynamical context for the amplitude biases identified earlier and motivate further examination of rainfall intensity distributions.

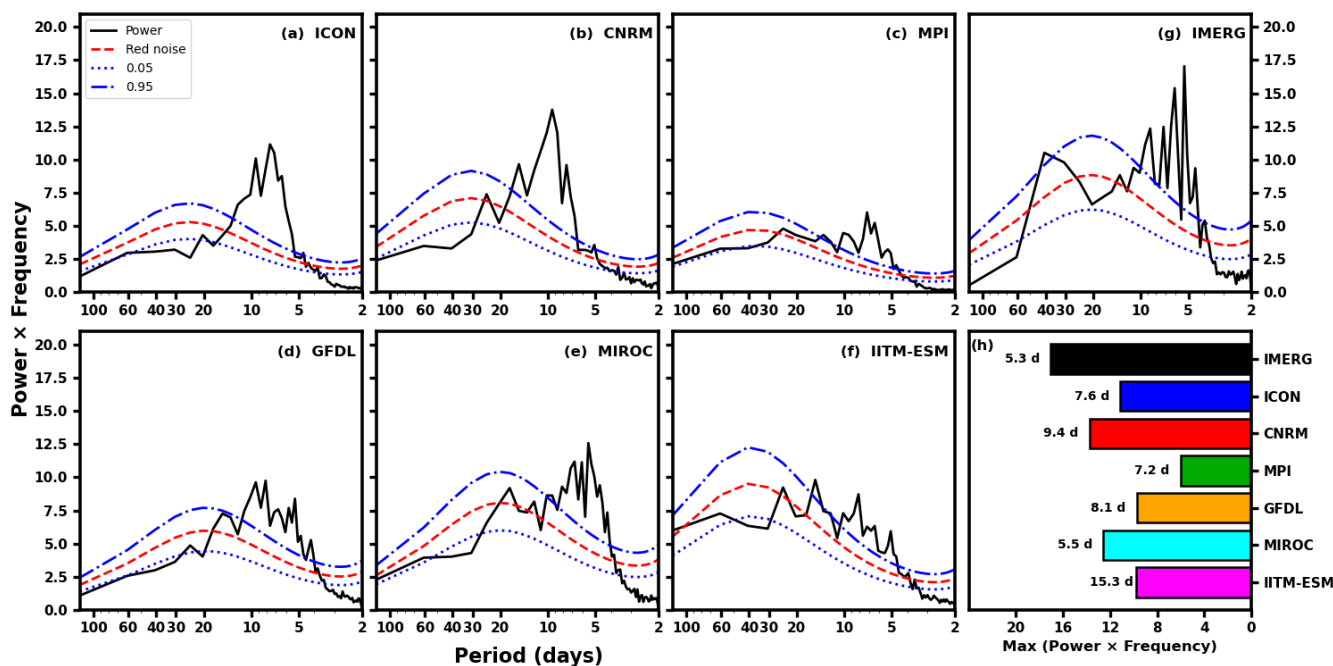


Figure 8. Composite power spectra of JJAS mean daily rainfall anomalies averaged over Indian region 10° – 25° N, 80° – 100° E (box ref: Saha et al., 2014) from (a-f) ICON, CNRM, MPI, GFDL, MIROC, and IITM-ESM, with (g) IMERG as observational references. The dashed blue curves denote the 5% and 95% confidence levels, and the red dashed curve represents the theoretical red-noise spectrum. Panel (h) summarizes the dominant period and corresponding peak spectral power for IMERG and all models

To complement the spectral analysis, we examine the probability density function (PDF) of daily rainfall to assess how differences in temporal variability translate into biases in rainfall intensity and frequency across models.

3.2.2 Probability Density Function (PDF)

425 The PDF analysis was performed over the CI region using each model’s native grid resolution. The PDF values were normalized by the total number of grid points within each rainfall bin, ensuring a consistent statistical comparison across models and observations. The Fig 9 is divided into three panels: the main panel displays rainfall intensities between 0 and 20 mm day^{-1} , while the two inset panels extend the range to 20–60 mm day^{-1} and 60–100 mm day^{-1} , respectively.

430 A common feature across most models is an enhanced frequency of light rainfall events (0 – 2 mm day^{-1}) relative to IMERG, indicative of the well-documented “drizzle bias” associated with parameterized convection (Chen et al., 2021; Dai, 2006; Stephens et al., 2010), although observational uncertainties in light rainfall retrievals remain (Prakash and Srinivasan, 2021). The higher-resolution models (ICON, CNRM, and MPI) exhibit particularly elevated occurrence of weak precipitation, suggesting frequent triggering of shallow or weakly organized convection. In contrast, the coarser-resolution models (GFDL and MIROC) show comparatively reduced drizzle frequency, while IITM-ESM ($\approx 190 \text{ km}$) slightly underestimates light rainfall

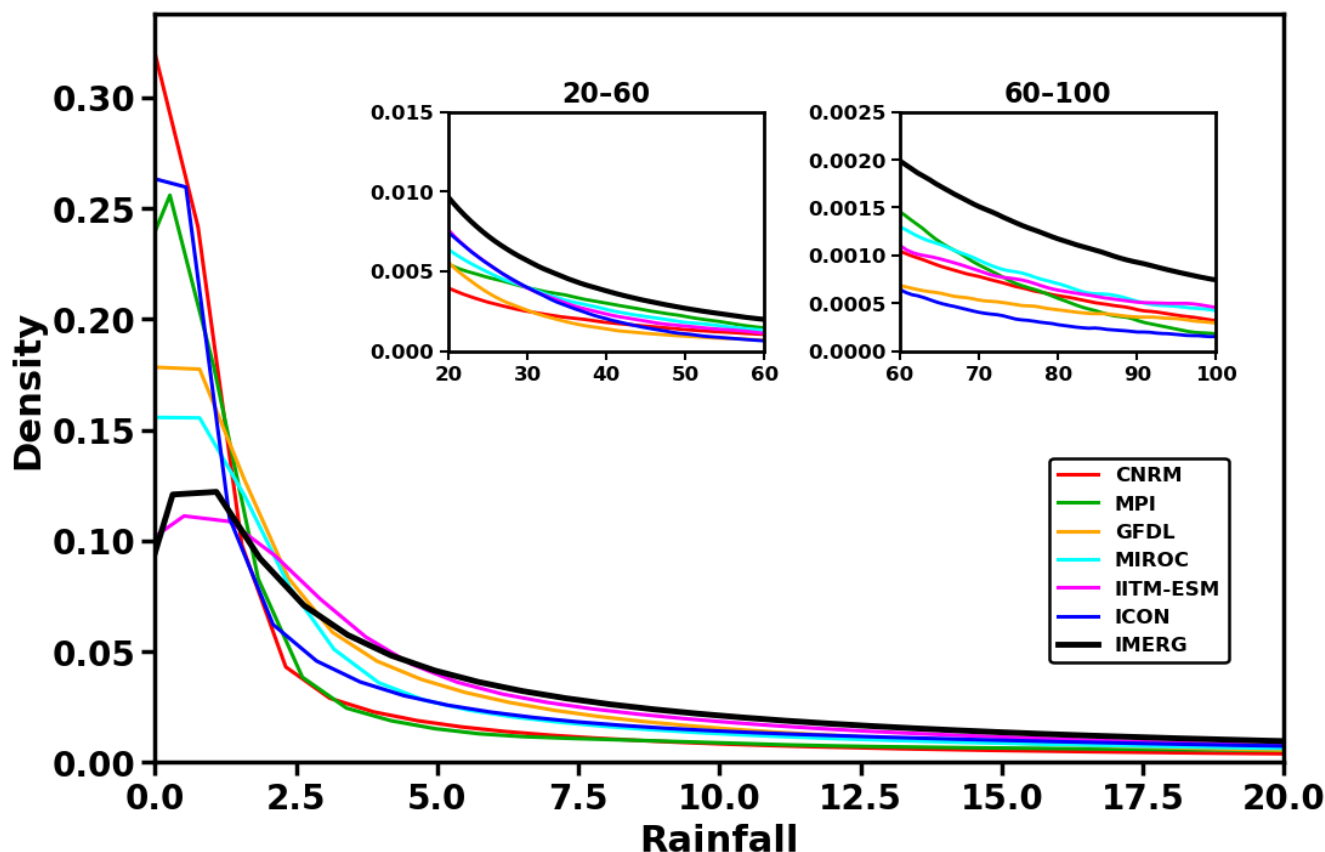


Figure 9. Probability density function (PDF) of JJAS daily rainfall over Central India from ICON and CMIP6 models (CNRM, MPI, GFDL, MIROC, and IITM-ESM), compared with IMERG. The main panel shows 0–20 mm day^{-1} , with inset panels extending to 20–60 mm day^{-1} and 60–100 mm day^{-1} .

435 and aligns more closely with IMERG in this narrow range. Beyond light intensities, systematic underestimation of moderate-to-heavy rainfall becomes evident across nearly all models. IMERG consistently shows higher probability across the 5–100 mm day^{-1} range, underscoring a general model tendency to underrepresent organized and intense convective events. Between 5 and 30 mm day^{-1} , ICON produces higher occurrence than CNRM and MPI but lower than GFDL and MIROC. In the 20–30 mm day^{-1} range, ICON shows the largest frequency among the higher-resolution models, though its distribution declines rapidly beyond 30 mm day^{-1} . MPI exhibits comparatively larger frequency in the 30–70 mm day^{-1} range, whereas MIROC extends the heavy-rainfall tail into the 70–100 mm day^{-1} band, though with lower overall probability than IMERG. Across the 2.5–15 mm day^{-1} range, coarser models dominate, reflecting a shift of rainfall occurrence toward moderate intensities.

445 These resolution-dependent differences likely arise from contrasting representations of convective organization and grid-scale averaging. At higher resolutions, increased triggering of parameterized convection can lead to frequent but weak rainfall



events, thereby enhancing light-rain probabilities while limiting moisture buildup required for intense precipitation (Dai, 2006; Stephens et al., 2010). Conversely, coarse grids spatially smooth rainfall and may artificially aggregate convective activity into moderate intensities, while still underrepresenting extreme events due to limited representation of mesoscale convective systems (MCSs) and subgrid variability (Kendon et al., 2012; Prein et al., 2015). Additionally, the inability of parameterized
450 convection to capture cold-pool dynamics, slantwise overturning circulations within organized MCSs (Moncrieff, 2019), and upscale growth of convective systems can suppress the heavy-rainfall tail across models.

Overall, the PDFs indicate a systematic redistribution of rainfall toward light-to-moderate intensities and a consistent underrepresentation of heavy rainfall events. When viewed alongside the spectral analysis, these distributional biases reinforce the conclusion that deficiencies in convective parameterization and mesoscale organization affect both the temporal variance and
455 intensity structure of monsoon rainfall. Such biases at daily scales can propagate upward, influencing synoptic aggregation and intraseasonal variability.

3.2.3 Rainfall Variance

The spatial distribution of band-pass filtered rainfall variance in the synoptic (2–7 days) and intraseasonal (10–20 and 20–100 days) bands delineates the regions where these modes are most active and provides insight into the underlying dynamical
460 processes that organize monsoon rainfall. Together, these three frequency bands account for the bulk of the seasonal variability of the Indian Summer Monsoon Rainfall (ISMR), as demonstrated by Saha et al. (2014). Fig 10 presents the variance computed from filtered daily rainfall anomalies across these bands, while Supplementary Fig S2 complements the spatial analysis by summarizing the PCC and RMSE of each model relative to IMERG, thereby enabling a quantitative evaluation of model skill across temporal scales.

465 In IMERG (Fig 10g), the synoptic band accounts for the largest share of seasonal variance ($\sim 190 \text{ mm}^2 \text{ day}^{-2}$), with pronounced maxima along the climatological monsoon trough extending from CI to the head BoB, and secondary centres over the Arabian Sea and Himalayan foothills. This distribution reflects the genesis and westward propagation of monsoon lows and depressions embedded within the trough circulation, as well as terrain-modulated convection along the Western Ghats and Himalayan foothills (e.g. Goswami et al., 2003). The enhanced synoptic variance over the eastern equatorial Indian
470 Ocean likely arises from convectively coupled equatorial wave activity and its interaction with the background monsoon flow, which organizes convection at 2–7 day timescales and contributes to the initiation of larger-scale variability. At intraseasonal timescales, the 10–20 (Fig 10n) and 20–100 (Fig 10u) day bands exhibit broadly similar spatial structures, highlighting the multiscale envelope of monsoon variability. Variance maxima remain anchored along the monsoon trough and the head BoB, while the equatorial Indian Ocean emerges as a key centre, particularly in the 20–100 day band consistent with the genesis
475 region of the monsoon intraseasonal oscillation (MISO), which subsequently propagates northward over the subcontinent (e.g. Sikka, 1977; Saha et al., 2014). The enhancement of variance over the equatorial Indian Ocean at 20–100 days underscores the coupled ocean–atmosphere processes central to large-scale intraseasonal organization.

Across models, the gross spatial organization is reproduced, but amplitude and regional fidelity vary. In the synoptic band, both IITM-ESM and CNRM shows the highest spatial agreement with IMERG (PCC ≈ 0.66 and 0.65 respectively) and

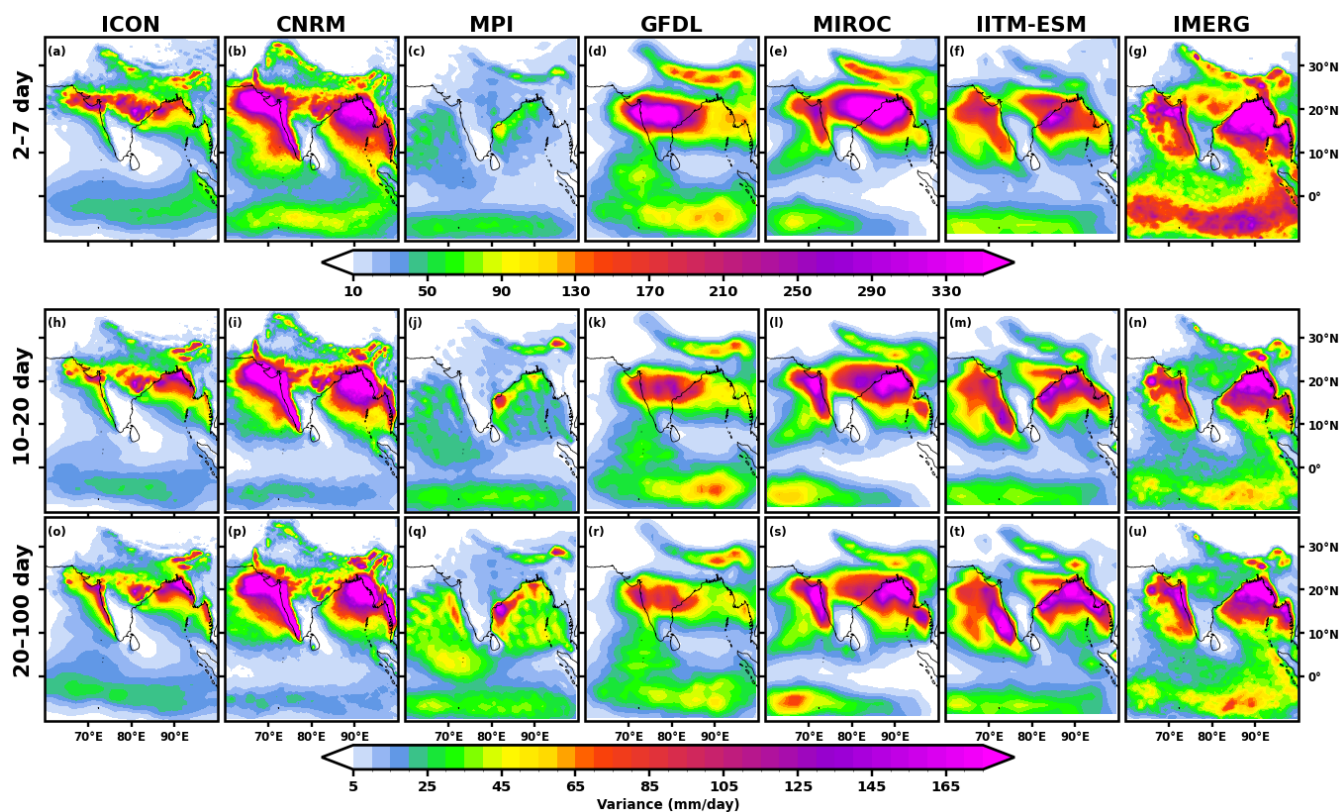


Figure 10. Climatological JJAS rainfall variance in synoptic (2–7 days), higher frequency ISO (10–20 days) and lower frequency ISO (20–100 days) band using filtered daily rainfall anomaly (in $\text{mm}^2 \text{day}^{-2}$) from ICON, all the participant CMIP6 (CNRM, MPI, GFDL, MIROC, and IITM-ESM) model simulations, and IMERG as observational reference.

480 lowest RMSE ($\sim 80 \text{ mm}^2 \text{day}^{-2}$) among other models. They are closely followed by MIROC ($\text{PCC} \approx 0.58$; $\text{RMSE} \approx 90 \text{ mm}^2 \text{day}^{-2}$). ICON captures the correct trough-aligned structure but with moderate amplitude underestimation, especially over oceanic and orographic regions ($\text{PCC} \approx 0.56$; $\text{RMSE} \approx 130 \text{ mm}^2 \text{day}^{-2}$). MPI substantially underestimates variance and misrepresents the trough orientation, while GFDL reproduce the large-scale structure but show moderate displacement of oceanic maxima. Consistent with observation, most models exhibit broadly similar spatial variance distributions in the

485 10–20 and 20–100 day bands. The primary distinction emerges over the equatorial Indian Ocean, where variance intensifies in the 20–100 day band, consistent with the genesis region of the MISO. An exception is MPI, which produces unrealistically large 20–100 day variance across all ocean basins (Arabian Sea, Bay of Bengal, and equatorial Indian Ocean), suggesting an over-amplified low-frequency oceanic signal. In the 10–20 day band, MIROC exhibits the highest spatial fidelity ($\text{PCC} \approx 0.78$), followed by ICON and IITM-ESM ($\text{PCC} \approx 0.74$). In terms of RMSE, the coarser-resolution models (e.g. MIROC

490 and IITM-ESM) show smaller errors, with RMSE values ($\sim 20 \text{ mm}^2 \text{day}^{-2}$) nearly half of ICON's, primarily due to ICON's underestimation of oceanic variance. In the 20–100 day band, MIROC again attains the highest PCC (~ 0.80), followed by



ICON (~ 0.78) and then by IITM-ESM and CNRM (~ 0.70). Here too higher resolution model (ICON and CNRM) has higher RMSE ($\sim 42 \text{ mm}^2 \text{ day}^{-2}$). The higher RMSE in ICON is consistent with its enhanced variance in the intraseasonal band, as also noted by (Pothapakula et al., 2026), who reported higher variability across multiple resolutions (10, 40, and 80 km) over the CI region. The remaining models cluster at substantially lower correlations and higher errors, indicating weaker spatial fidelity and amplitude biases in representing intraseasonal variability.

Synoptic-scale variance is most realistically represented by IITM-ESM and CNRM, whereas MIROC consistently leads in both intraseasonal bands, with ICON performing competitively and IITM-ESM slightly behind at longer timescales. Although most models reproduce the broad spatial organization of multiscale variance, systematic amplitude biases persist, especially over the equatorial Indian Ocean and monsoon trough core regions. These discrepancies underscore ongoing challenges in representing the dynamical coupling between monsoon depressions, ocean–atmosphere feedbacks, and large-scale intraseasonal convection, highlighting the importance of accurately simulating multiscale interactions within the monsoon system

3.2.4 Rainfall seasonal mean

The seasonal mean rainfall represents the combined effect of processes across shorter timescales from diurnal convection to synoptic systems and ISOs, thereby representing the cumulative outcome of all mechanisms that shape monsoon rainfall. Thus, the seasonal mean serves as an integrated test of model performance, indicating whether skill at shorter timescales translates into realistic seasonal accumulation or whether multiscale biases amplify into systematic errors.

In IMERG (Fig 11g), the seasonal rainfall pattern aligns closely with the previously identified variance hotspots. Regions characterized by strong synoptic activity and terrain-modulated convection—such as the monsoon trough corridor and major orographic belts—emerge as the principal rainfall maxima. Likewise, the equatorial Indian Ocean, highlighted earlier as a center of intraseasonal variance and MISO genesis (e.g. Yasunari, 1979; Saha et al., 2014), contributes substantially to seasonal accumulation through persistent large-scale convergence and low-frequency modulation. Thus, the climatological mean reflects the spatial imprint of multiscale convective organization rather than independent large-scale forcing alone.

Model performance at the seasonal scale largely reflects their variance characteristics, while the bias patterns (Fig S3) clarify how systematic biases accumulate spatially. ICON (Fig 11a) maintains strong spatial coherence with IMERG (PCC = 0.85; RMSE = 2.3 mm day^{-1}), indicating that its relatively balanced representation of synoptic and intraseasonal variability translates into a realistic seasonal rainfall structure. Its bias field exhibits a weak dipole over land, with alternating wet and dry anomalies across central and peninsular India, while oceanic deviations remain modest (generally within $\pm 3 \text{ mm day}^{-1}$). The limited amplitude of these biases suggests that residual multiscale errors are not strongly amplified in the seasonal integration.

CNRM (Fig 11b) shows reasonable spatial alignment (PCC ≈ 0.65 – 0.70 ; RMSE $\approx 5 \text{ mm day}^{-1}$) but overestimates rainfall along the Western Ghats and parts of the monsoon trough while underestimating over sections of the equatorial Indian Ocean, consistent with its enhanced land-based variance and comparatively weaker low-frequency oceanic variability. MPI (Fig 11c) displays weak spatial skill (PCC ≈ 0.1 ; RMSE $\approx 5.5 \text{ mm day}^{-1}$), with widespread oceanic wet biases and dry bias over monsoon trough region, reflecting its excessive low-frequency oceanic variance.

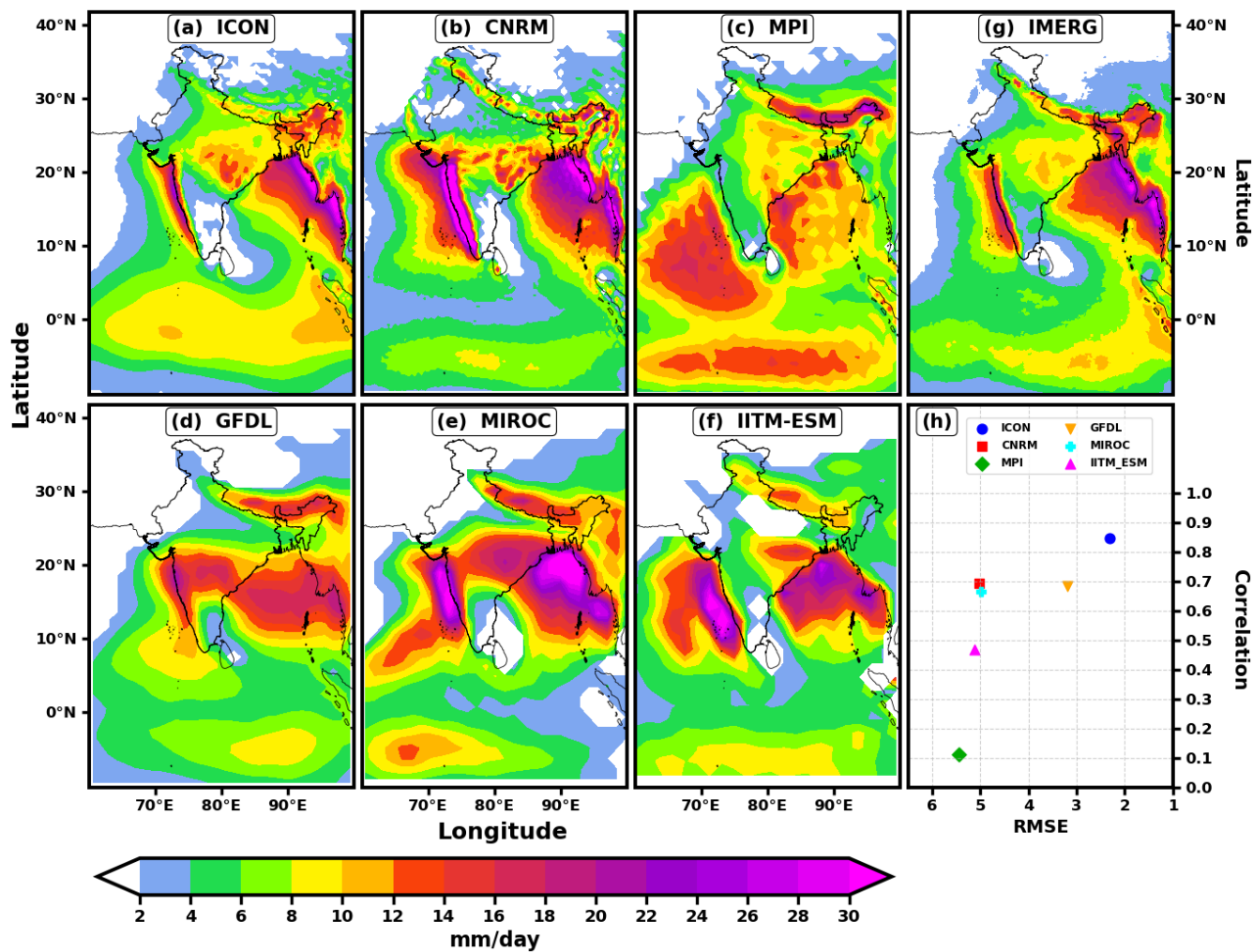


Figure 11. Seasonal (JJAS) averaged climatological mean rainfall (in mm day^{-1}) from (a) ICON, all the participant CMIP6 (b-f: CNRM, MPI, GFDL, MIROC, and IITM-ESM) model simulations, and IMERG (g) as observational reference. Panel (h) shows the scatter between pattern correlation and RMSE.



525 Among the coarser-resolution models, GFDL and MIROC (Fig 11d,e) display contrasting but systematic bias signatures. GFDL ($PCC \approx 0.65\text{--}0.70$; $RMSE \approx 3.2 \text{ mm day}^{-1}$) shows a dry bias along the monsoon trough and head BoB but wet anomalies over the Arabian Sea and southern BoB. MIROC, while capturing the broad monsoon envelope, exhibits pronounced wet biases over the Arabian Sea and BoB and a substantial dry bias over the eastern equatorial Indian Ocean, contributing to higher RMSE. These opposing tendencies are consistent with their differing representations of oceanic variance amplitude identified in the previous section. However, IITM-ESM (Fig 11f) occupies an intermediate position, with alternating wet and 530 dry anomalies along the trough and a marked wet bias over the Arabian Sea coupled with dry conditions over the equatorial Indian Ocean, indicating persistent land–ocean amplitude imbalance despite good synoptic variance skill.

Overall, the seasonal climatology reinforces the multiscale diagnostics: models that more realistically represent synoptic and intraseasonal organization tend to better reproduce the integrated monsoon rainfall pattern. However, systematic oceanic 535 overestimation and regional amplitude biases demonstrate that variance errors do not average out but project coherently onto the seasonal mean. Accurate simulation of ISMR therefore depends critically on balanced cross-scale interactions rather than correct seasonal circulation alone.

3.2.5 Annual Rainfall

The seasonal mean rainfall highlighted the accumulated imprint of multiscale variability and the annual cycle, in contrast, 540 reveals its temporal evolution. By tracing the onset, northward migration, peak, and withdrawal of the monsoon rainband, it provides a dynamic view of how the seasonal state develops. Here we discuss the latitude–time evolution over $70^\circ\text{--}90^\circ\text{E}$, enabling assessment of each model’s ability to capture the timing, amplitude, and meridional progression of monsoon rainfall. Most models capture this northward migration pattern with varying degrees of accuracy. Earlier model generations often failed to simulate this evolution realistically (e.g. Pokhrel et al., 2018a).

545 IMERG (Fig 12g) clearly captures three distinct rainfall regimes: equatorial precipitation maxima during the pre-monsoon (April–May) and post-monsoon (October–November) seasons, and a pronounced northward migration of convection reaching 25°N during JJAS. This meridional shift reflects the seasonal transition from the OTCZ to the Continental Tropical Convergence Zone (CTCZ), a defining characteristic of the dynamical large-scale monsoon system and closely linked to monsoon intraseasonal variability. The latitude of maximum rainfall (shown in a overlaid black line) remains anchored over the Indian 550 mainland throughout JJAS before retreating southward in September, marking the observed withdrawal phase.

Most models reproduce the broad northward migration, though with systematic differences in amplitude and timing. Earlier model generations often struggled to simulate this seasonal evolution realistically (e.g. Pokhrel et al., 2018a), but several CMIP6 models and ICON show notable improvement in capturing the transition between oceanic and continental convection. ICON most faithfully reproduces both the seasonal progression and the September withdrawal, consistent with IMERG. In 555 contrast, MPI allows rainfall to extend north of 25°N but retains its core maximum near 15°N , indicating weaker continental convection and excessive OTCZ rainfall; its withdrawal occurs prematurely around July. CNRM, GFDL, MIROC, and IITM-ESM generally overestimate rainfall within the CTCZ while underestimating OTCZ intensity, and most simulate a delayed retreat in October rather than September. Quantitatively, the PCC–RMSE analysis (Fig 12h) confirms ICON’s superior per-



560 formance ($PCC = 0.88$; $RMSE = 2.0 \text{ mm day}^{-1}$), followed by GFDL ($PCC = 0.78$; $RMSE = 2.5 \text{ mm day}^{-1}$), while the remaining models cluster within $PCC = 0.65\text{--}0.74$ and $RMSE = 3.2\text{--}3.9 \text{ mm day}^{-1}$.

To further assess seasonal phase evolution, the domain-averaged annual cycle over the Indian land region is examined (Fig S4). Over land, all models reproduce the observed unimodal structure. ICON and GFDL best simulate onset and peak timing during July–August; however, ICON shows slightly early withdrawal, whereas GFDL exhibits a broader seasonal extent with delayed retreat. MPI closely follows in structure but underestimates peak intensity. CNRM and MIROC overestimate peak rainfall, while IITM-ESM substantially underestimates it. The Taylor diagram (Fig S4d) reflects this hierarchy: ICON, GFDL, and MPI cluster with 0.99 correlation and realistic variance, whereas MIROC and CNRM overestimate variance by 20–30%, and IITM-ESM underestimates it by 20%.

570 Over the extended monsoon region—including adjacent oceanic areas—all models tend to produce higher rainfall than IMERG observations (Fig S4a). MPI exhibits the largest positive bias, driven by excessive oceanic rainfall despite weaker land precipitation. GFDL shows a wet bias extending beyond September, consistent with its delayed withdrawal. Most models display a broader seasonal distribution than observed, suggesting early onset and/or late retreat tendencies. ICON again remains closest to observations, capturing both seasonal progression and peak intensity. This is corroborated by the Taylor plot (Fig S4c), where ICON shows 0.99 correlation and accurately reproduces observed variance, closely followed by GFDL (correlation = 0.98). CNRM slightly overestimates variance (correlation = 0.91), while IITM-ESM, MPI, and MIROC overestimate variance 575 by approximately 30%, 45%, and 50%, respectively, despite relatively high correlations (0.96–0.98).

Thus, the annual cycle analysis confirms that a multiscale perspective is essential for interpreting monsoon simulation fidelity. Models that maintain balanced land–ocean variance and realistic intraseasonal evolution more accurately reproduce the seasonal migration and timely withdrawal of the monsoon rainband. In contrast, oceanic magnitude biases and phase errors at intraseasonal timescales lead to premature retreat, broadened seasonal extent, or exaggerated peak intensity in the annual cycle. 580 These results show that realistic monsoon simulation depends on consistent cross-scale organization, as errors in variability do not disappear through seasonal averaging but instead project directly onto the evolving seasonal structure.

3.3 Multiscale Rainfall Biases

Do the systematic rainfall biases identified at individual timescales translate into scale-dependent variance biases relative to IMERG? Moreover, does such redistribution differ between land and ocean, where distinct dynamical controls operate? To 585 address these questions, this section examines how models redistribute monsoon variability from higher to lower frequencies using area-averaged diagnostics over two representative regions, CI and the BoB (as shown in Fig 13f), capturing the contrasting continental and oceanic regimes.

Over CI, variance biases shows how the models redistribute their continental convective variability across scales. ICON maintains the most balanced structure, with deviations largely within $\pm 50\%$, slightly underestimating synoptic variance while 590 modestly enhancing intraseasonal variability. This aligns with earlier findings that it captures the spatial organization of monsoon LPS but underestimates their intensity (e.g. Deoras et al., 2021).

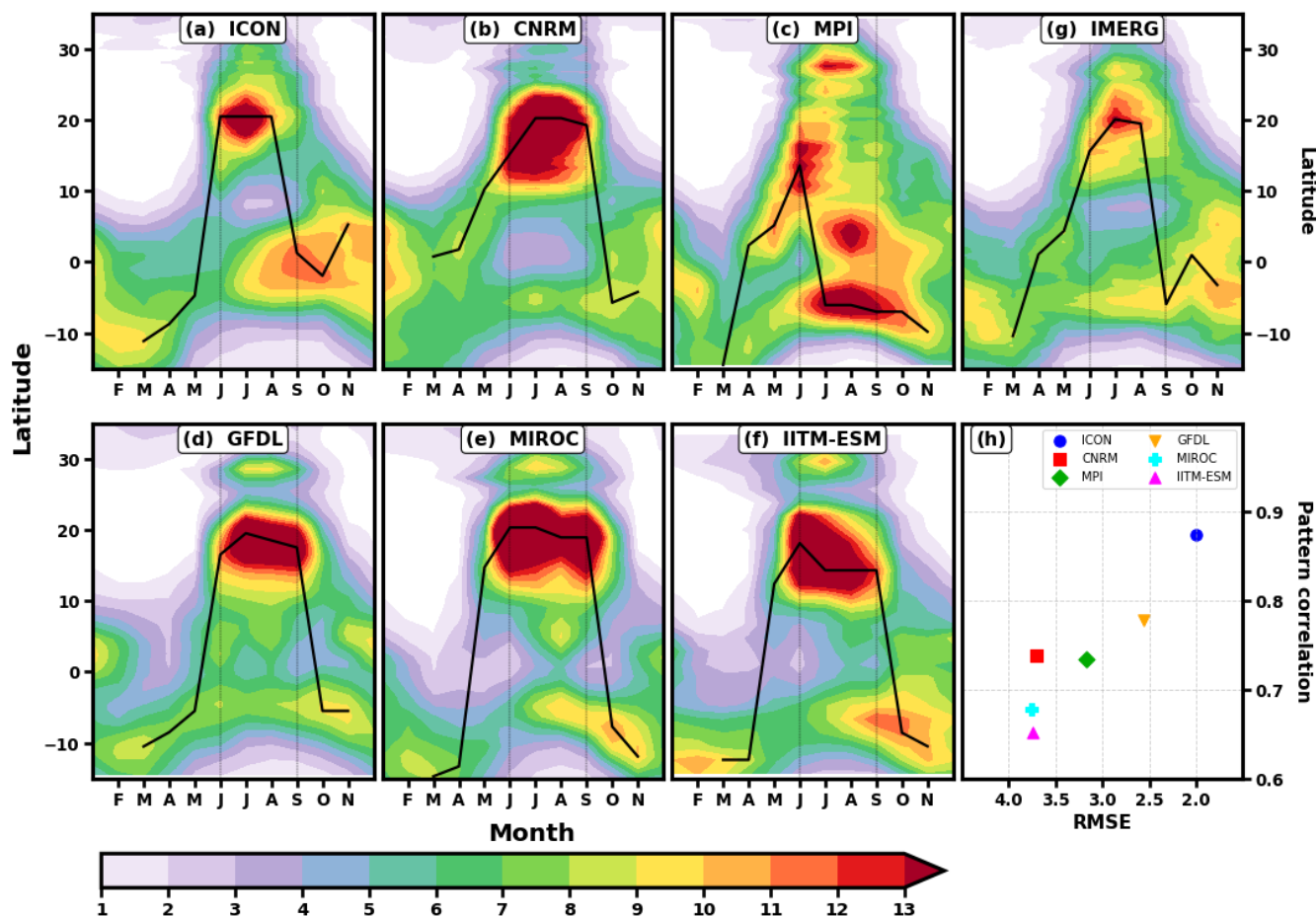


Figure 12. Latitude–time evolution of the climatological mean annual cycle of precipitation (mm day^{-1}) averaged zonally over the Indian monsoon region (70° – 90°E) from (a–f) ICON, CNRM, MPI, GFDL, MIROC, and IITM-ESM model simulations, with (g) IMERG as observational reference. The overlaid black curve denotes the latitude of maximum precipitation, illustrating the seasonal migration of the monsoon rainband. The faint black dotted lines mark the monsoon season (JJAS). Panel (h) presents the scatter of pattern correlation coefficient (PCC) versus root-mean-square error (RMSE) for all models relative to IMERG.



MPI, in contrast, shows extreme amplification of diurnal variance ($>600\%$), corresponding to an excess of $\sim 48 \text{ mm}^2 \text{ day}^{-2}$ relative to the observed $\sim 8 \text{ mm}^2 \text{ day}^{-2}$, as also seen in Fig 2 where it showed the largest diurnal amplitude bias among all models. This behaviour is consistent with excessive high-frequency convection and the well-known “drizzling bias” in global models (Dai, 2006; Zhou et al., 2008; Chen et al., 2021), often linked to premature triggering of deep convection during boundary-layer growth over heated land surfaces. Notably, although both MPI and ICON employ mass-flux–based convective parameterizations, their diurnal biases differ markedly. MPI strongly overestimates land diurnal variance, whereas ICON remains comparatively controlled over land. This contrast suggests that diurnal variance errors arise not from the parameterization framework alone, but from how it interacts with land–atmosphere coupling processes. Most other models, meanwhile, suppress diurnal variance over land, indicating weakened high-frequency convective organization. At synoptic and intraseasonal scales, GFDL and MIROC tend to amplify organized variability, whereas IITM-ESM exhibit more moderate, scale-dependent biases.

Thus, over land, inter-model divergence primarily reflects how energy is partitioned between diurnal convection and organized synoptic–intraseasonal disturbances, shaping the seasonal rainfall structure discussed earlier.

Over the BoB, the bias structure shifts, underscoring the dominant role of ocean–atmosphere interaction. ICON exhibits a pronounced positive diurnal variance bias ($\sim 180\%$, $\sim 54 \text{ mm}^2 \text{ day}^{-2}$ relative to the observed $\sim 30 \text{ mm}^2 \text{ day}^{-2}$), consistent with its enhanced oceanic diurnal amplitude noted previously. Unlike over land, this amplification likely reflects an over-responsive coupling of convection to low-level moisture convergence under prescribed SST conditions. In strongly coupled oceanic regions such as the BoB, the absence of two-way air–sea feedback in AMIP simulations can exaggerate atmospheric variability (Pegion and Kirtman, 2008; DeMott et al., 2014). At synoptic and intraseasonal scales, ICON’s biases turn negative but remain within $\pm 60\%$, indicating relatively realistic organized variability despite enhanced high-frequency convection. Among CMIP6 models, IITM-ESM shows the strongest amplification at lower frequencies, with $\sim 100\%$ positive bias in the 20–100 day band (an excess of $\sim 160 \text{ mm}^2 \text{ day}^{-2}$ relative to the observed $\sim 80 \text{ mm}^2 \text{ day}^{-2}$), followed by $\sim 60\%$ in the 10–20 day band and $\sim 40\%$ in the synoptic band, while suppressing diurnal variance ($\sim 50\%$). MIROC exhibits a similar but slightly weaker enhancement of intraseasonal variance ($\sim 80\%$ in 10–20 day and $\sim 50\%$ in synoptic bands). In contrast, MPI and CNRM generally suppress synoptic and intraseasonal variability over the ocean, while GFDL remains comparatively balanced, with most biases within $\pm 10\%$ except for a $\sim 50\%$ reduction in diurnal variance.

The land–ocean contrast is therefore clear: over land, variance biases are dominated by errors in diurnal–synoptic partitioning and boundary-layer convection coupling, whereas over the ocean, biases primarily reflect misrepresentation of intraseasonal modulation and air–sea interaction. These systematic variance imbalances set the stage for the amplitude biases in the phase-locked diurnal and seasonal cycles discussed next.

Fig 14 isolates rainfall amplitude biases at the two phase-locked endpoints of the temporal spectrum—diurnal and seasonal scales—thereby complementing the variance redistribution diagnosed in Fig 13. Because these scales are locked to the diurnal and annual cycles, respectively, amplitude biases provide a direct measure of systematic intensity errors rather than variability redistribution.

Over land, ICON exhibits modest amplitude biases at both diurnal and seasonal scales (within $\sim 5\text{--}10\%$), consistent with its relatively balanced multiscale variance structure. In contrast, MPI shows a pronounced overestimation of diurnal amplitude

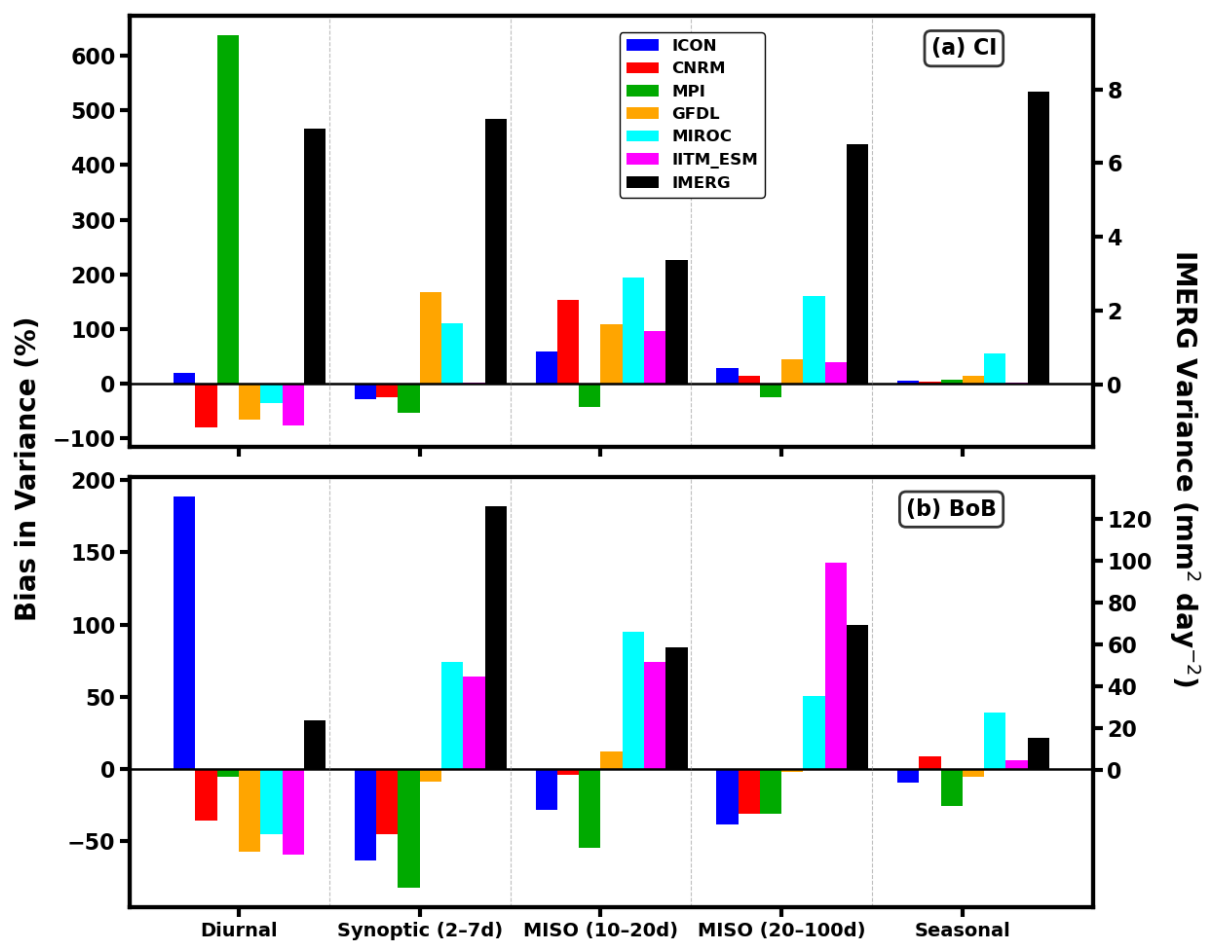


Figure 13. Percentage climatological JJAS rainfall variance bias relative to IMERG, computed as $[(\sigma_{\text{model}}^2 - \sigma_{\text{IMERG}}^2) / \sigma_{\text{IMERG}}^2] \times 100$, for the diurnal, synoptic, higher frequency MISO (10–20 days), lower frequency MISO (20–100 days), and seasonal (JJAS) bands. Results are shown for ICON and CMIP6 AMIP models (CNRM, MPI, GFDL, MIROC, and IITM-ESM) over (a) Central India (CI) and (b) Bay of Bengal (BoB) region. The analysis domains are indicated in Fig 2 .

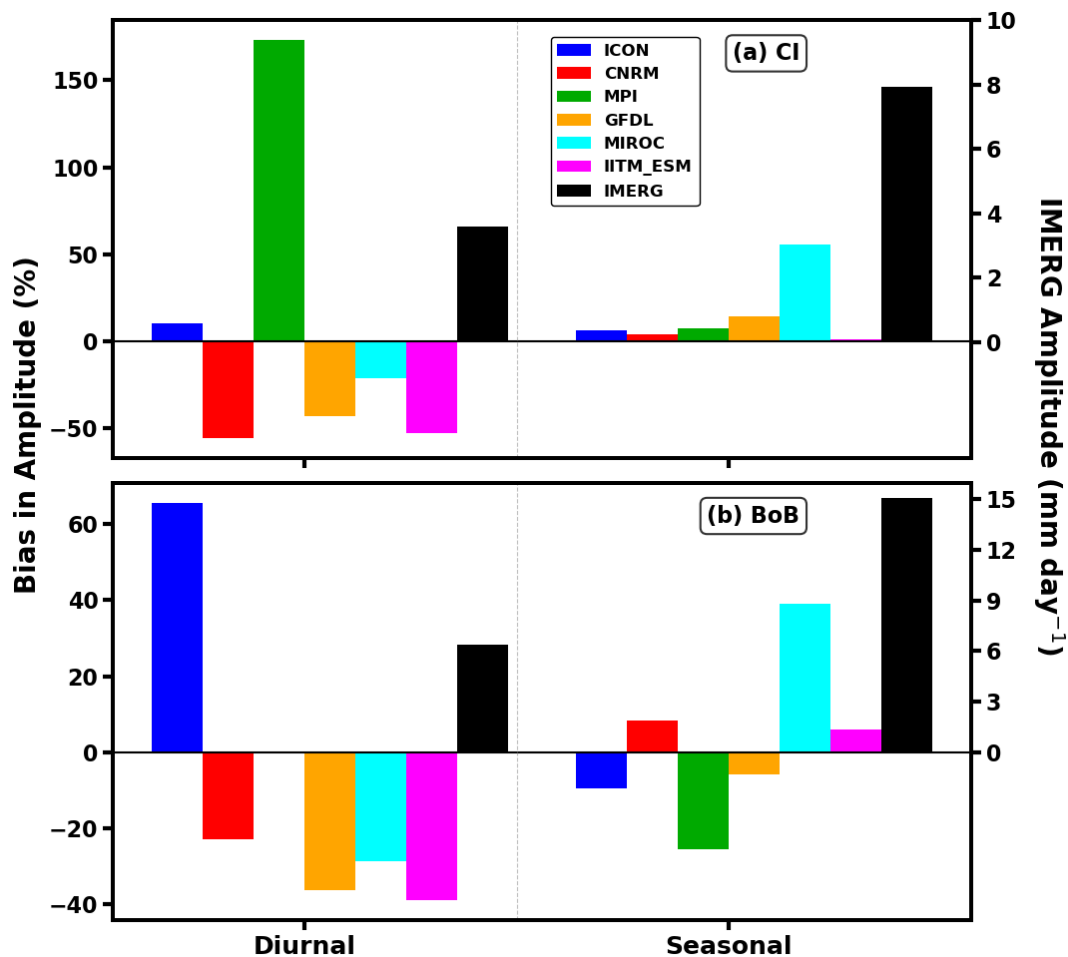


Figure 14. Same as Fig 13, but for percentage climatological JJAS rainfall amplitude bias relative to IMERG at the diurnal and seasonal (JJAS) timescales, which are phase-locked to the diurnal and annual cycles, respectively.

(>150%), directly mirroring its excessive diurnal variance and reflecting overly sensitive convective triggering within a mass-flux framework. The remaining models (CNRM, GFDL, MIROC, and IITM-ESM) generally underestimate diurnal amplitude, with the largest reduction in CNRM (~50%, corresponding to ~2 mm day⁻¹ relative to an observed ~4 mm day⁻¹). Notably, these sub-daily amplitude errors substantially diminish at the seasonal scale, indicating that much of the diurnal bias averages out over the monsoon period. An exception is MIROC, which exhibits a stronger seasonal amplitude bias (~50%, ~4 mm day⁻¹), consistent with its enhanced lower-frequency variance discussed earlier.

Over the ocean, ICON displays a strong positive diurnal amplitude bias (~60%) over the BoB, reinforcing the large diurnal variance excess identified in Fig 13 and its earlier diagnosed diurnal rainfall enhancement. This behavior likely reflects limitations of the AMIP configuration, where prescribed SSTs may exaggerate atmospheric responsiveness in strongly coupled



regions. As over land, ICON's amplitude bias reduces substantially at the seasonal scale. Most other CMIP6 models underestimate oceanic diurnal amplitude (10–40%, with MIROC showing the largest reduction), and seasonal biases generally decrease relative to diurnal errors, though MIROC and MPI retain noticeable seasonal-scale deviations.

640 Taken together, the amplitude diagnostics confirm that errors at the phase-locked endpoints influence how variance is re-distributed across intermediate scales. Models with exaggerated diurnal amplitude tend to distort higher-frequency variance, whereas amplified seasonal amplitude is linked to enhanced intraseasonal variability. Accurate simulation of these temporal endpoints is therefore essential for maintaining physically consistent multiscale monsoon rainfall behavior.

645 It is worth noting that the substantially larger diurnal variance bias relative to the amplitude bias (e.g., ~180% versus ~60% over the BoB in ICON) reflects the quadratic relationship between amplitude and variance. Because variance scales with the square of amplitude, even moderate increases in diurnal intensity can produce disproportionately large increases in variability. This indicates that the model enhances day-to-day fluctuations of the diurnal cycle more strongly than the mean diurnal rainfall amount itself, implying an over-responsive high-frequency convective adjustment rather than a simple uniform increase in rainfall

4 Summary and Conclusions

650 This study evaluates the capability of a medium-resolution (40 km), non-hydrostatic global model (ICON) to simulate ISMR arising from complex multiscale interactions spanning diurnal to seasonal timescales. ICON is examined as a test case for next-generation dynamical cores and is systematically compared with a suite of five CMIP6-class models (CNRM, MPI, GFDL, MIROC, and IITM-ESM) having horizontal resolutions from 50 to 190 km. All models are analyzed in AMIP configuration against high-resolution IMERG observations (~10 km) over a common 17-year period (1998–2014), allowing isolation of atmospheric sources of rainfall bias under prescribed SST forcing. The results reveal that monsoon rainfall errors are inherently multiscale and strongly shaped by land–ocean contrasts, indicating that biases emerge differently across convective, synoptic and seasonal regimes. At the diurnal scale, model behavior diverges sharply depending on convective formulation and surface coupling. ICON shows the most realistic continental diurnal cycle, with modest amplitude biases (~5-10%) and limited phase errors that allow coherent afternoon–evening convection over land. However, over the BoB it substantially overestimates diurnal amplitude (~60%) and variance (~180%). In the present 40 km configuration, these biases are likely linked to the convective parameterization (Tiedtke–Bechtold mass-flux scheme). Previous studies have shown that convective parameterizations in medium- to coarse-resolution climate models tend to produce overly frequent precipitation and exhibit strong sensitivity to low-level moisture convergence, leading to excessive rainfall and an amplified diurnal cycle (e.g. Tao et al., 2023; Christopoulos and Schneider, 2021). While studies based on convection-permitting (~2.5 km) ICON configurations attribute similar oceanic wet biases to overactive warm-cloud microphysics and excessive rainfall from shallow and congestus clouds (Prein et al., 2026), such mechanisms might not directly applicable here due to the reliance on parameterized convection at coarser resolution.

665 MPI exhibits the strongest land diurnal bias, with amplitude overestimation exceeding 150% and an early rainfall phase. These errors arise because convection remains unresolved even at higher resolution, leaving rainfall characteristics largely



controlled by resolution-insensitive parameterizations (Hertwig et al., 2015). Previous studies have also reported an over-
670 estimation of convective rainfall over the Indian region in earlier versions of MPI (Chaudhari et al., 2019), consistent with the
excessive amplitude seen here. Increasing resolution primarily redistributes rainfall between convective and large-scale compo-
nents without improving its timing or magnitude. Consequently, the bias reflects deficiencies in sub-grid cloud and convection
schemes, including inadequate triggering and biased cloud representation that distort radiative forcing and the precipitation
cycle (Stevens et al., 2013). Over ocean, MPI underestimates diurnal variability, indicating weak nocturnal convective organi-
675 zation. CNRM shows premature daytime triggering over land and failure to initiate nocturnal convection above the boundary
layer, resulting in weakened evening rainfall (Watters et al., 2021) and over ocean, its relatively smaller phase errors sug-
gest somewhat improved nocturnal organization, though amplitude biases persist. The similar early land convection in GFDL
is consistent with its strict quasi-equilibrium closure that neglects non-equilibrium shallow convection, while its nocturnal
rainfall deficit reflects missing cold-pool dynamics and mesoscale lifting processes (Zhang et al., 2024) and over ocean, addi-
680 tional biases arise from boundary-layer and cloud microphysics deficiencies, affecting radiative balance and marine convection
(Donner et al., 2011).

In MIROC6, biases in precipitation timing and intensity primarily arise from convection parameterizations. Despite the
introduction of shallow convection schemes to enhance moisture mixing and reduce low-level cloud biases, these remain
key tuning factors for rainfall distribution. Persistent deficiencies in vertical moisture mixing and convective triggering lead
685 to timing errors, including an unrealistically early precipitation peak (Tatebe et al., 2019). IITM-ESM biases stem from its
relatively coarse horizontal resolution ($\sim 2^\circ$) and limitations in cloud and convection parameterizations. Despite improvements
from the revised Simplified Arakawa–Schubert (RSAS) scheme, deficiencies in cloud microphysics contribute to a persistent
dry bias. Previous studies have also documented a tendency of SAS and RSAS based schemes to produce dry biases over
the Indian land region (e.g. Pokhrel et al., 2016; Swapna et al., 2018). In addition, inaccuracies in humidity fields and large-
690 scale tropical circulation weaken moisture transport and convergence, compounded by the poor representation of key regional
circulation features essential for realistic monsoon rainfall (Prajeesh et al., 2022). These deficiencies likely contribute to a
weaker and less well-phased diurnal cycle in the model.

Together, these results demonstrate that diurnal rainfall biases are not determined by parameterization framework alone, but
by its interaction with land–atmosphere and air–sea processes.

695 At synoptic timescales (2–7 days), observed variance over land is dominated by monsoon low-pressure systems and mesoscale
convective systems. ICON maintains realistic spatial organization, though with slightly reduced magnitude, suggesting moder-
ate suppression of organized disturbances. MPI, in contrast, substantially suppresses synoptic variability, consistent with weak
representation of organized disturbance growth. The remaining models either redistribute excessive power into intermediate
(10–20 day) bands or fail to sustain coherent synoptic-scale evolution. Over the ocean, a similar tendency emerges, with several
700 models underestimating synoptic variance, indicating weak organization of marine convective systems and limited maintenance
of large-scale disturbances.

At intraseasonal scales (10–20 and 20–100 days), deficiencies become more systematic, with many CMIP6 models known
to exhibit conspicuous phase shifts in low-frequency 30–60 day ISOs that lead to artificially extended early-season dry spells



(Singh, 2023). Over land, variance redistribution differs across models but remains secondary to oceanic errors. Over the
705 BoB and equatorial Indian Ocean, most models underestimate the 20–100-day band by ~30–60%, highlighting the inability of
AMIP configurations to sustain coupled MISO dynamics without ocean feedback. Coarser-resolution models tend to amplify
intermediate (10–20 day) bands, whereas higher-resolution configurations often underestimate low-frequency variability. These
scale-dependent imbalances influence seasonal rainfall accumulation and migration.

Seasonal rainfall emerges as the cumulative imprint of these multiscale imbalances. Models maintaining proportionate en-
710 ergy partitioning across scales, most notably ICON shows strong spatial agreement with IMERG ($PCC \approx 0.85$; $RMSE \approx 2.3$
 mm day^{-1}) and realistic annual migration, including September withdrawal. GFDL also performs reasonably well, though
with a slightly broader seasonal extent. MPI underestimates synoptic variability and shows early withdrawal in the annual
cycle. MIROC and IITM-ESM exhibit enhanced intermediate-frequency variance that contributes to seasonal amplitude distor-
tions (approaching ~40–50% in some regions). CNRM maintains reasonable timing but overestimates rainfall over key oceanic
715 regions. Amplitude diagnostics indicate that diurnal amplitude biases generally reduce at the seasonal scale, suggesting that
sub-daily intensity errors partly average out over the monsoon season. However, models with enhanced intermediate-frequency
variance retain noticeable seasonal amplitude deviations.

This study demonstrates that credible monsoon simulation depends less on seasonal-mean accuracy alone and more on
maintaining physically consistent cross-scale organization. While non-hydrostatic dynamics at 40 km contribute to improved
720 continental convection, ICON's performance also reflects its well-tuned physical parameterizations, benefiting from its devel-
opment within a numerical weather prediction framework, which enables a more realistic representation of mesoscale pro-
cesses and their interactions with larger scale circulation. However, persistent oceanic biases highlight remaining challenges
in convective organization, cloud microphysics, and air–sea coupling. Across the CMIP6 ensemble, biases in convective trig-
gering, shallow-to-deep transition, mesoscale system organization, and boundary-layer–radiative coupling are likely to play an
important role in shaping the fidelity of scale interactions. Future progress requires explicit diagnosing of cross-scale interac-
725 tions rather than scale-isolated evaluation. Approaches such as Multivariate Empirical Mode Decomposition (MEMD) offer a
promising framework to diagnose nonlinear variability redistribution among diurnal, synoptic, and intraseasonal modes. Such
scale-aware diagnostics can help distinguish locally generated errors from those arising through multiscale interaction, pro-
viding targeted guidance for improving convective parameterizations, boundary-layer processes, microphysics, and coupled
730 ocean–atmosphere representation. Advancing these diagnostics is essential for achieving physically consistent and societally
relevant prediction of the Indian Summer Monsoon across weather-to-climate timescales.

Data availability. The data listed in Section 2 and Table 1 that support the findings of this study are openly available except for ICON. Data
website links are given below:

- GPM-IMERG: https://disc.gsfc.nasa.gov/datasets/GPM_3IMERGHH_07/summary?keywords=%22IMERG%20final%22
- 735 – CMIP6: <https://esgf-node.ornl.gov/search>
- ICON: <https://doi.org/10.5281/zenodo.17250248>



Supplement. The supplementary files contain additional four supporting figures for this study.

Author contributions. SP, VU, and PKS conceptualized the study and developed the methodology, performed the formal analysis, validated and reviewed the results, and wrote, reviewed, and edited the manuscript. SKS reviewed the results and contributed to writing, reviewing, and editing the manuscript. PPK designed ICON experiments and conducted simulations under AP and AD supervision at ETH Zürich. AS organized collaborative meetings and participated in scientific discussions. All the authors reviewed the manuscript. SY, HC, AR, NG, KPP, and HR reviewed and edited the manuscript draft.

Competing interests. The authors declare that they have no competing interests.

Acknowledgements. We extend our sincere thanks to the Ministry of Earth Sciences (MoES); Indian Institute of Tropical Meteorology (IITM); Savitribai Phule Pune University; AcSIR; and the HPC support team for their invaluable assistance in carrying out this study. We also gratefully acknowledge the support from EXCLAIM project at ETH Zurich for providing the platform to conduct simulations with a refactored GT4Py dynamical core version of ICON. The Swiss Super Computing Centre (CSCS) is acknowledged for providing computational resources on ALPS supercomputer. We thank the executive committee Nicolas Gruber, Thomas Schulthess, Oliver Fuhrer, Andreas F. Prein and Christoph Schär of EXCLAIM for their support in ICON model development. We further thank the editor and the anonymous reviewers for their constructive comments and helpful suggestions.



References

- Annamalai, H. and Slingo, J. M.: Active/break cycles: diagnosis of the intraseasonal variability of the Asian Summer Monsoon, *Climate Dynamics*, 18, 85–102, <https://doi.org/10.1007/s003820100161>, 2001.
- Asensio, H., Messmer, M., Lüthi, D., and Osterried, K.: External Parameters for Numerical Weather Prediction and Climate Application (EXTPAR v5_0): User and Implementation Guide, ETH Zürich and COSMO Consortium, http://www.cosmo-model.org/content/support/software/ethz/EXTPAR_user_and_implementation_manual_202003.pdf, [Accessed 2025], 2020.
- 755 Baranowski, D. B., Waliser, D. E., Jiang, X., Ridout, J. A., and Flatau, M. K.: Contemporary GCM Fidelity in Representing the Diurnal Cycle of Precipitation Over the Maritime Continent, *Journal of Geophysical Research: Atmospheres*, 124, 747–769, <https://doi.org/https://doi.org/10.1029/2018JD029474>, 2019.
- 760 Barros, A. P. and Lang, T. J.: Monitoring the Monsoon in the Himalayas: Observations in Central Nepal, June 2001, *Monthly Weather Review*, 131, 1408 – 1427, [https://doi.org/10.1175/1520-0493\(2003\)131<1408:MTMITH>2.0.CO;2](https://doi.org/10.1175/1520-0493(2003)131<1408:MTMITH>2.0.CO;2), 2003.
- Basu, B. K.: Diurnal variation in precipitation over India during the summer monsoon season: observed and model predicted, *Monthly Weather Review*, 135, 2155–2167, <https://doi.org/10.1175/MWR3355.1>, 2007.
- Bechtold, P., Bazile, E., Guichard, F., Mascart, P., and Richard, E.: A mass-flux convection scheme for regional and global models, *Quarterly Journal of the Royal Meteorological Society*, 127, 869–886, <https://doi.org/https://doi.org/10.1002/qj.49712757309>, 2001.
- 765 Bechtold, P., Chaboureau, J.-P., Beljaars, A., Betts, A. K., Köhler, M., Miller, M., and Redelsperger, J.-L.: The simulation of the diurnal cycle of convective precipitation over land in a global model, *Quarterly Journal of the Royal Meteorological Society*, 130, 3119–3137, <https://doi.org/https://doi.org/10.1256/qj.03.103>, 2004.
- Bechtold, P., Köhler, M., Jung, T., Doblas-Reyes, F., Leutbecher, M., Rodwell, M. J., Vitart, F., and Balsamo, G.: Advances in simulating atmospheric variability with the ECMWF model: From synoptic to decadal time-scales, *Quarterly Journal of the Royal Meteorological Society*, 134, 1337–1351, <https://doi.org/https://doi.org/10.1002/qj.289>, 2008.
- 770 Betts, A. K. and Jakob, C.: Evaluation of the diurnal cycle of precipitation, surface thermodynamics, and surface fluxes in the ECMWF model using LBA data, *Journal of Geophysical Research: Atmospheres*, 107, LBA 12–1–LBA 12–8, <https://doi.org/https://doi.org/10.1029/2001JD000427>, 2002.
- 775 Bretherton, C. S., McCaa, J. R., and Grenier, H.: A New Parameterization for Shallow Cumulus Convection and Its Application to Marine Subtropical Cloud-Topped Boundary Layers. Part I: Description and 1D Results, *Monthly Weather Review*, 132, 864 – 882, [https://doi.org/10.1175/1520-0493\(2004\)132<0864:ANPFSC>2.0.CO;2](https://doi.org/10.1175/1520-0493(2004)132<0864:ANPFSC>2.0.CO;2), 2004.
- Chaudhari, H. S., Hazra, A., Pokhrel, S., Saha, S. K., and Talluri, S. S.: Simulation of extreme Indian summer monsoon years in Coupled Model Intercomparison Project Phase 5 models: Role of cloud processes, *International Journal of Climatology*, 39, 901–920, <https://doi.org/https://doi.org/10.1002/joc.5851>, 2019.
- 780 Chen, D., Dai, A., and Hall, A.: The Convective-To-Total Precipitation Ratio and the “Drizzling” Bias in Climate Models, *Journal of Geophysical Research: Atmospheres*, 126, e2020JD034198, <https://doi.org/https://doi.org/10.1029/2020JD034198>, 2021.
- Chen, G.: Diurnal Cycle of the Asian Summer Monsoon: Air Pump of the Second Kind, *Journal of Climate*, 33, 1747 – 1775, <https://doi.org/10.1175/JCLI-D-19-0210.1>, 2020.
- 785 Chikira, M. and Sugiyama, M.: A Cumulus Parameterization with State-Dependent Entrainment Rate. Part I: Description and Sensitivity to Temperature and Humidity Profiles, *Journal of the Atmospheric Sciences*, 67, 2171 – 2193, <https://doi.org/10.1175/2010JAS3316.1>, 2010.



- Christopoulos, C. and Schneider, T.: Assessing Biases and Climate Implications of the Diurnal Precipitation Cycle in Climate Models, *Geophysical Research Letters*, 48, e2021GL093017, <https://doi.org/https://doi.org/10.1029/2021GL093017>, 2021.
- Chutia, T., Chakraborty, A., Bhat, G. S., and Rajeevan, M.: Shifted Diurnal Cycle of Indian Summer Monsoon Rainfall, *Geophysical Research Letters*, 52, e2025GL116401, <https://doi.org/https://doi.org/10.1029/2025GL116401>, 2025.
- 790 Dai, A.: Precipitation Characteristics in Eighteen Coupled Climate Models, *Journal of Climate*, 19, 4605 – 4630, <https://doi.org/10.1175/JCLI3884.1>, 2006.
- Dai, A. and Trenberth, K. E.: The Diurnal Cycle and Its Depiction in the Community Climate System Model, *Journal of Climate*, 17, 930 – 951, [https://doi.org/10.1175/1520-0442\(2004\)017<0930:TDCAID>2.0.CO;2](https://doi.org/10.1175/1520-0442(2004)017<0930:TDCAID>2.0.CO;2), 2004.
- 795 DeMott, C. A., Stan, C., Randall, D. A., and Branson, M. D.: Intraseasonal Variability in Coupled GCMs: The Roles of Ocean Feedbacks and Model Physics, *Journal of Climate*, 27, 4970 – 4995, <https://doi.org/10.1175/JCLI-D-13-00760.1>, 2014.
- Deoras, A., Hunt, K. M. R., and Turner, A. G.: Comparison of the Prediction of Indian Monsoon Low Pressure Systems by Subseasonal-to-Seasonal Prediction Models, *Weather and Forecasting*, 36, 859 – 877, <https://doi.org/10.1175/WAF-D-20-0081.1>, 2021.
- Dipankar, A., Bianco, M., Bukenberger, M., Ehrenguber, T., Farabullini, N., Fuhrer, O., Gopal, A., Hupp, D., Jocksch, A., Kellerhals, S., Kroll, C. A., Lapillonne, X., Leclair, M., Luz, M., Müller, C., Ong, C. R., Osuna, C., Pothapakula, P., Prein, A., Röthlin, M., Sawyer, W., Schär, C., Schemm, S., Serafini, G., Vogt, H., Weber, B., Wills, R. C. J., Gruber, N., and Schulthess, T. C.: Toward exascale climate modelling: a python DSL approach to ICON's (icosahedral non-hydrostatic) dynamical core (icon-exclaim v0.2.0), *Geoscientific Model Development*, 19, 713–729, <https://doi.org/10.5194/gmd-19-713-2026>, 2026.
- 800 Donner, L. J., Wyman, B. L., Hemler, R. S., Horowitz, L. W., Ming, Y., Zhao, M., Golaz, J.-C., Ginoux, P., Lin, S.-J., Schwarzkopf, M. D., Austin, J., Alaka, G., Cooke, W. F., Delworth, T. L., Freidenreich, S. M., Gordon, C. T., Griffies, S. M., Held, I. M., Hurlin, W. J., Klein, S. A., Knutson, T. R., Langenhorst, A. R., Lee, H.-C., Lin, Y., Magi, B. I., Malyshev, S. L., Milly, P. C. D., Naik, V., Nath, M. J., Pincus, R., Ploshay, J. J., Ramaswamy, V., Seman, C. J., Shevliakova, E., Sirutis, J. J., Stern, W. F., Stouffer, R. J., Wilson, R. J., Winton, M., Wittenberg, A. T., and Zeng, F.: The Dynamical Core, Physical Parameterizations, and Basic Simulation Characteristics of the Atmospheric Component AM3 of the GFDL Global Coupled Model CM3, *Journal of Climate*, 24, 3484 – 3519, <https://doi.org/10.1175/2011JCLI3955.1>, 2011.
- 815 Emanuel, K. A.: *Atmospheric Convection*, Oxford University Press, New York, 1994.
- Folkens, I., Mitovski, T., and Pierce, J. R.: A simple way to improve the diurnal cycle in convective rainfall over land in climate models, *Journal of Geophysical Research: Atmospheres*, 119, 2113–2130, <https://doi.org/https://doi.org/10.1002/2013JD020149>, 2014.
- Fujinami, H., Nomura, S., and Yasunari, T.: Characteristics of Diurnal Variations in Convection and Precipitation over the Southern Tibetan Plateau during Summer, *SOLA*, 1, 49–52, <https://doi.org/10.2151/sola.2005-014>, 2005.
- Godbole, R. V.: The composite structure of the monsoon depression, *Tellus*, <https://doi.org/10.3402/tellusa.v29i1.11327>, 1977.
- Goswami, B. N., Keshavamurty, R. N., and Satyan, V.: Role of barotropic, baroclinic and combined barotropic-baroclinic instability for the growth of monsoon depressions and mid-tropospheric cyclones, *Proceedings of the Indian Academy of Sciences - Earth and Planetary Sciences*, 89, 79–97, <https://doi.org/10.1007/BF02841521>, 1980.
- 820 Goswami, B. N., Ajayamohan, R. S., Xavier, P. K., and Sengupta, D.: Clustering of synoptic activity by Indian summer monsoon intraseasonal oscillations, *Geophysical Research Letters*, 30, <https://doi.org/https://doi.org/10.1029/2002GL016734>, 2003.
- Goswami, B. N., Venugopal, V., Sengupta, D., Madhusoodanan, M. S., and Xavier, P. K.: Increasing Trend of Extreme Rain Events Over India in a Warming Environment, *Science*, 314, 1442–1445, <https://doi.org/10.1126/science.1132027>, 2006.



- 825 Guo, H., John, J. G., Blanton, C., McHugh, C., Nikonov, S., Radhakrishnan, A., Rand, K., Zadeh, N. T., Balaji, V., Durachta, J., Dupuis, C., Menzel, R., Robinson, T., Underwood, S., Vahlenkamp, H., Bushuk, M., Dunne, K. A., Dussin, R., Gauthier, P. P., Ginoux, P., Griffies, S. M., Hallberg, R., Harrison, M., Hurlin, W., Lin, P., Malyshev, S., Naik, V., Paulot, F., Paynter, D. J., Ploshay, J., Reichl, B. G., Schwarzkopf, D. M., Seman, C. J., Shao, A., Silvers, L., Wyman, B., Yan, X., Zeng, Y., Adcroft, A., Dunne, J. P., Held, I. M., Krasting, J. P., Horowitz, L. W., Milly, P., Shevliakova, E., Winton, M., Zhao, M., and Zhang, R.: NOAA-GFDL GFDL-CM4 model output amip, <https://doi.org/10.22033/ESGF/CMIP6.8494>, 2018.
- 830 GUÉRÉMY, J. F.: A continuous buoyancy based convection scheme: one- and three-dimensional validation, *Tellus A*, 63, 687–706, <https://doi.org/https://doi.org/10.1111/j.1600-0870.2011.00521.x>, 2011.
- Hajima, T., Abe, M., Arakawa, O., Suzuki, T., Komuro, Y., Ogura, T., Ogochi, K., Watanabe, M., Yamamoto, A., Tatebe, H., Noguchi, M. A., Ohgaito, R., Ito, A., Yamazaki, D., Ito, A., Takata, K., Watanabe, S., Kawamiya, M., and Tachiiri, K.: MIROC MIROC-ES2L model output prepared for CMIP6 CMIP amip, <https://doi.org/10.22033/ESGF/CMIP6.5421>, 2020.
- 835 Han, J. and Pan, H.-L.: Revision of Convection and Vertical Diffusion Schemes in the NCEP Global Forecast System, *Weather and Forecasting*, 26, 520 – 533, <https://doi.org/10.1175/WAF-D-10-05038.1>, 2011.
- Hannachi, A., Jolliffe, I. T., and Stephenson, D. B.: Empirical orthogonal functions and related techniques in atmospheric science: A review, *International Journal of Climatology*, 27, 1119–1152, <https://doi.org/https://doi.org/10.1002/joc.1499>, 2007.
- Held, I. M., Guo, H., Adcroft, A., Dunne, J. P., Horowitz, L. W., Krasting, J., Shevliakova, E., Winton, M., Zhao, M., Bushuk, M., Wittenberg, 840 A. T., Wyman, B., Xiang, B., Zhang, R., Anderson, W., Balaji, V., Donner, L., Dunne, K., Durachta, J., Gauthier, P. P. G., Ginoux, P., Golaz, J.-C., Griffies, S. M., Hallberg, R., Harris, L., Harrison, M., Hurlin, W., John, J., Lin, P., Lin, S.-J., Malyshev, S., Menzel, R., Milly, P. C. D., Ming, Y., Naik, V., Paynter, D., Paulot, F., Ramaswamy, V., Reichl, B., Robinson, T., Rosati, A., Seman, C., Silvers, L. G., Underwood, S., and Zadeh, N.: Structure and Performance of GFDL's CM4.0 Climate Model, *Journal of Advances in Modeling Earth Systems*, 11, 3691–3727, <https://doi.org/https://doi.org/10.1029/2019MS001829>, 2019.
- 845 Hertwig, E., von Storch, J.-S., Handorf, D., et al.: Effect of horizontal resolution on ECHAM6-AMIP performance, *Climate Dynamics*, 45, 185–211, <https://doi.org/10.1007/s00382-014-2396-x>, 2015.
- Hong, S.-Y. and Lim, J.-O. J.: The WRF single-moment 6-class microphysics scheme (WSM6), *Journal of the Korean Meteorological Society*, 42, 129–151, 2006.
- Houze Jr., R. A.: Mesoscale convective systems, *Reviews of Geophysics*, 42, <https://doi.org/https://doi.org/10.1029/2004RG000150>, 2004.
- 850 Huang, W.-R. and Wang, S.-Y. S.: Future changes in propagating and non-propagating diurnal rainfall over East Asia, *Climate Dynamics*, 49, 375–389, <https://doi.org/10.1007/s00382-016-3348-4>, 2017.
- Huffman, G. J., Stocker, E. F., Bolvin, D. T., Nelkin, E. J., and Tan, J.: GPM IMERG Final Precipitation L3 Half Hourly 0.1 degree x 0.1 degree V07, <https://doi.org/10.5067/GPM/IMERG/3B-HH/07>, [Accessed 2025], 2023.
- Hunt, K. M. R. and Turner, A. G.: Non-linear intensification of monsoon low-pressure systems by the BSISO, *Weather and Climate Dynam-* 855 *ics*, 3, 1341–1358, <https://doi.org/10.5194/wcd-3-1341-2022>, 2022.
- Hunt, K. M. R., Turner, A. G., and Schiemann, R. K. H.: Katabatic and convective processes drive two preferred peaks in the precipitation diurnal cycle over the Central Himalaya, *Quarterly Journal of the Royal Meteorological Society*, 148, 1731–1751, <https://doi.org/https://doi.org/10.1002/qj.4275>, 2022.
- Jha, A. K., Das, S. K., Krishna, U. V. M., and Deshpande, S. M.: Role of Thermodynamics and Dynamics in the Diurnal Cycle, Propagation, 860 and Progression of Convective Storms in the Eastern Flank of the Indian Monsoon Trough, *Journal of the Atmospheric Sciences*, 79, 3351 – 3374, <https://doi.org/10.1175/JAS-D-21-0159.1>, 2022.



- Jiang, X., Adames, Á. F., Kim, D., Maloney, E. D., Lin, H., Kim, H., Zhang, C., DeMott, C. A., and Klingaman, N. P.: Fifty Years of Research on the Madden-Julian Oscillation: Recent Progress, Challenges, and Perspectives, *Journal of Geophysical Research: Atmospheres*, 125, e2019JD030911, <https://doi.org/https://doi.org/10.1029/2019JD030911>, 2020.
- 865 Johnson, R. H.: Diurnal Cycle of Monsoon Convection, pp. 257–276, https://doi.org/10.1142/9789814343411_0015, 2011.
- Jungclaus, J., Bittner, M., Wieners, K.-H., Wachsmann, F., Schupfner, M., Legutke, S., Giorgetta, M., Reick, C., Gayler, V., Haak, H., de Vrese, P., Raddatz, T., Esch, M., Mauritsen, T., von Storch, J.-S., Behrens, J., Brovkin, V., Claussen, M., Crueger, T., Fast, I., Fiedler, S., Hagemann, S., Hohenegger, C., Jahns, T., Kloster, S., Kinne, S., Lasslop, G., Kornblueh, L., Marotzke, J., Matei, D., Meraner, K., Mikolajewicz, U., Modali, K., Müller, W., Nabel, J., Notz, D., Peters-von Gehlen, K., Pincus, R., Pohlmann, H., Pongratz, J., Rast, S., 870 Schmidt, H., Schnur, R., Schulzweida, U., Six, K., Stevens, B., Voigt, A., and Roeckner, E.: MPI-M MPI-ESM1.2-HR model output prepared for CMIP6 CMIP amip, <https://doi.org/10.22033/ESGF/CMIP6.6463>, 2019.
- Kendon, E. J., Roberts, N. M., Senior, C. A., and Roberts, M. J.: Realism of Rainfall in a Very High-Resolution Regional Climate Model, *Journal of Climate*, 25, 5791 – 5806, <https://doi.org/10.1175/JCLI-D-11-00562.1>, 2012.
- Kikuchi, K. and Wang, B.: Diurnal Precipitation Regimes in the Global Tropics, *Journal of Climate*, 21, 2680 – 2696, 875 <https://doi.org/10.1175/2007JCLI2051.1>, 2008.
- Kilpatrick, T., Xie, S.-P., and Nasuno, T.: Diurnal Convection-Wind Coupling in the Bay of Bengal, *Journal of Geophysical Research: Atmospheres*, 122, 9705–9720, <https://doi.org/https://doi.org/10.1002/2017JD027271>, 2017.
- Kinne, S.: The MACv2 aerosol climatology, *Tellus B: Chemical and Physical Meteorology*, 71, 1–21, 2019.
- Konda, G. and Vissa, N. K.: Robustness of BSISO and air-sea interactions in the CMIP (Phase-6) models over the North Indian Ocean, 880 *Dynamics of Atmospheres and Oceans*, 99, 101–136, <https://doi.org/https://doi.org/10.1016/j.dynatmoce.2022.101316>, 2022.
- Krishna, U. V., Das, S. K., Deshpande, S. M., and Pandithurai, G.: Physical processes controlling the diurnal cycle of convective storms in the Western Ghats, *Scientific Reports*, 11, 2045–2322, <https://doi.org/10.1038/s41598-021-93173-0>, 2021.
- Krishnamurti, T. N. and Bhalme, H. N.: Oscillations of a Monsoon System. Part I. Observational Aspects, *Journal of Atmospheric Sciences*, 33, 1937 – 1954, [https://doi.org/10.1175/1520-0469\(1976\)033<1937:OOAMSP>2.0.CO;2](https://doi.org/10.1175/1520-0469(1976)033<1937:OOAMSP>2.0.CO;2), 1976.
- 885 Krishnamurti, T. N. and Subrahmanyam, D.: The 30–50 Day Mode at 850 mb During MONEX, *Journal of Atmospheric Sciences*, 39, 2088 – 2095, [https://doi.org/10.1175/1520-0469\(1982\)039<2088:TDMAMD>2.0.CO;2](https://doi.org/10.1175/1520-0469(1982)039<2088:TDMAMD>2.0.CO;2), 1982.
- Krishnamurti, T. N., Gnanaseelan, C., and Chakraborty, A.: Prediction of the Diurnal Change Using a Multimodel Superensemble. Part I: Precipitation, *Monthly Weather Review*, 135, 3613 – 3632, <https://doi.org/10.1175/MWR3446.1>, 2007.
- Krishnan, R., Swapna, P., Vellore, R., Narayanasetti, S., Prajeesh, A. G., Choudhury, A. D., Singh, M., Sabin, T. P., and Sanjay, J.: The IITM 890 Earth System Model (ESM): Development and Future Roadmap, pp. 183–195, Springer Singapore, Singapore, ISBN 978-981-13-3396-5, https://doi.org/10.1007/978-981-13-3396-5_9, 2019.
- Lapillonne, X., Hupp, D., Gessler, F., Walser, A., Pauling, A., Lauber, A., Cumming, B., Osuna, C., Müller, C., Merker, C., Leuenberger, D., Leutwyler, D., Alexeev, D., Vollenweider, G., Van Parys, G., Jucker, J., Jansing, L., Arpagaus, M., Induni, M., Jacob, M., Kraushaar, M., Jähn, M., Stellio, M., Fuhrer, O., Baumann, P., Steiner, P., Kaufmann, P., Dietlicher, R., Müller, R., Kosukhin, S., Schulthess, T. C., 895 Schättler, U., Cherkas, V., and Sawyer, W.: Operational numerical weather prediction with ICON on GPUs (version 2024.10), *Geoscientific Model Development*, 19, 755–772, <https://doi.org/10.5194/gmd-19-755-2026>, 2026.
- Lee, Y.-C. and Wang, Y.-C.: Evaluating Diurnal Rainfall Signal Performance from CMIP5 to CMIP6, *Journal of Climate*, 34, 7607 – 7623, <https://doi.org/10.1175/JCLI-D-20-0812.1>, 2021.



- Leuenberger, D., Koller, M., Fuhrer, O., and Schär, C.: A Generalization of the SLEVE Vertical Coordinate, *Monthly Weather Review*, 138, 3683 – 3689, <https://doi.org/10.1175/2010MWR3307.1>, 2010.
- Lin, X., Randall, D. A., and Fowler, L. D.: Diurnal Variability of the Hydrologic Cycle and Radiative Fluxes: Comparisons between Observations and a GCM, *Journal of Climate*, 13, 4159 – 4179, [https://doi.org/10.1175/1520-0442\(2000\)013<4159:DVOTHC>2.0.CO;2](https://doi.org/10.1175/1520-0442(2000)013<4159:DVOTHC>2.0.CO;2), 2000.
- Lopez, P.: Implementation and validation of a new prognostic large-scale cloud and precipitation scheme for climate and data-assimilation purposes, *Quarterly Journal of the Royal Meteorological Society*, 128, 229–257, <https://doi.org/https://doi.org/10.1256/00359000260498879>, 2002.
- Lorenz, E. N.: Empirical Orthogonal Functions and Statistical Weather Prediction, Tech. Rep. Report 1, Statistical Forecasting Project, Massachusetts Institute of Technology, 1956.
- Mak, M.: Synoptic-scale disturbances in the summer monsoon, in: *Monsoon Meteorology*, edited by Chang, C. P. and Krishnamurti, T. N., pp. 435–460, Oxford University Press, New York, 1987.
- Mapes, B. E., Warner, T. T., and Xu, M.: Diurnal Patterns of Rainfall in Northwestern South America. Part III: Diurnal Gravity Waves and Nocturnal Convection Offshore, *Monthly Weather Review*, 131, 830 – 844, [https://doi.org/10.1175/1520-0493\(2003\)131<0830:DPORIN>2.0.CO;2](https://doi.org/10.1175/1520-0493(2003)131<0830:DPORIN>2.0.CO;2), 2003.
- Misra, V. and Jayasankar, C. B.: An observational study of the modulation of the diurnal variations by the intraseasonal oscillations of the Indian summer monsoon, *Climate Dynamics*, 64, 38, <https://doi.org/10.1007/s00382-025-08019-6>, 2026.
- Moncrieff, M. W.: Toward a Dynamical Foundation for Organized Convection Parameterization in GCMs, *Geophysical Research Letters*, 46, 14 103–14 108, <https://doi.org/https://doi.org/10.1029/2019GL085316>, 2019.
- Murali Krishna, U. V., Das, S. K., Deshpande, S. M., Doiphode, S. L., and Pandithurai, G.: The assessment of Global Precipitation Measurement estimates over the Indian subcontinent, *Earth and Space Science*, 4, 540–553, <https://doi.org/https://doi.org/10.1002/2017EA000285>, 2017.
- Müller, W. A., Jungclaus, J. H., Mauritsen, T., Baehr, J., Bittner, M., Budich, R., Bunzel, F., Esch, M., Ghosh, R., Haak, H., Ilyina, T., Kleine, T., Kornblüch, L., Li, H., Modali, K., Notz, D., Pohlmann, H., Roeckner, E., Stemmler, I., Tian, F., and Marotzke, J.: A Higher-resolution Version of the Max Planck Institute Earth System Model (MPI-ESM1.2-HR), *Journal of Advances in Modeling Earth Systems*, 10, 1383–1413, <https://doi.org/https://doi.org/10.1029/2017MS001217>, 2018.
- Müller, W. A., Früh, B., Korn, P., Pothast, R., Baehr, J., Bettems, J.-M., Bölöni, G., Brienen, S., Fröhlich, K., Helmert, J., Jungclaus, J., Köhler, M., Lorenz, S., Schneider, A., Schnur, R., Schulz, J.-P., Schlemmer, L., Sgoff, C., Pham, T. V., Pohlmann, H., Vogel, B., Vogel, H., Wirth, R., Zaehle, S., Zängl, G., Stevens, B., and Marotzke, J.: ICON: Toward Vertically Integrated Model Configurations for Numerical Weather Prediction, Climate Predictions, and Projections, *Bulletin of the American Meteorological Society*, 106, E1017 – E1031, <https://doi.org/10.1175/BAMS-D-24-0042.1>, 2025.
- N., G. B.: South Asian summer monsoon : An overview, *The Global Monsoon System : Research and Forecast*, <https://cir.nii.ac.jp/crid/1570572700527255040>, 2005.
- Narayanasetti, S., Panickal, S., Gopinathan, P. A., Choudhury, A. D., Singh, M., and Raghavan, K.: CCCR-IITM IITM-ESM model output prepared for CMIP6 ScenarioMIP ssp126, <https://doi.org/10.22033/ESGF/CMIP6.14747>, 2020.
- Park, S. and Bretherton, C. S.: The University of Washington Shallow Convection and Moist Turbulence Schemes and Their Impact on Climate Simulations with the Community Atmosphere Model, *Journal of Climate*, 22, 3449–3469, <https://doi.org/10.1175/2008JCLI2557.1>, 2009.



- Patwardhan, S., Sooraj, K. P., Varikoden, H., Vishnu, S., Koteswararao, K., Ramarao, M. V. S., and Pattanaik, D. R.: Synoptic Scale Systems, pp. 143–154, Springer Singapore, Singapore, ISBN 978-981-15-4327-2, https://doi.org/10.1007/978-981-15-4327-2_7, 2020.
- Pegion, K. and Kirtman, B. P.: The Impact of Air–Sea Interactions on the Simulation of Tropical Intraseasonal Variability, *Journal of Climate*, 21, 6616 – 6635, <https://doi.org/10.1175/2008JCLI2180.1>, 2008.
- 940 Peng, C.-H. and Chen, X.: Monsoonal MCS Initiation, Rainfall, and Diurnal Gravity Waves over the Bay of Bengal: Observation and a Linear Model, *Journal of the Atmospheric Sciences*, 81, 1401 – 1418, <https://doi.org/10.1175/JAS-D-23-0230.1>, 2024.
- Piriou, J.-M., Redelsperger, J.-L., Geleyn, J.-F., Lafore, J.-P., and Guichard, F.: An Approach for Convective Parameterization with Memory: Separating Microphysics and Transport in Grid-Scale Equations, *Journal of the Atmospheric Sciences*, 64, 4127 – 4139, 945 <https://doi.org/10.1175/2007JAS2144.1>, 2007.
- Pokhrel, S. and Sikka, D. R.: Variability of the TRMM-PR total and convective and stratiform rain fractions over the Indian region during the summer monsoon, *Climate Dynamics*, 41, 21–44, <https://doi.org/10.1007/s00382-012-1502-1>, 2013.
- Pokhrel, S., Saha, S. K., Dhakate, A., et al.: Seasonal prediction of Indian summer monsoon rainfall in NCEP CFSv2: Forecast and predictability error, *Climate Dynamics*, 46, 2305–2326, <https://doi.org/10.1007/s00382-015-2703-1>, 2016.
- 950 Pokhrel, S., Hazra, A., Chaudhari, H. S., Saha, S. K., Paulose, F., Krishna, S., Krishna, P. M., and Rao, S. A.: Hindcast skill improvement in Climate Forecast System (CFSv2) using modified cloud scheme, *International Journal of Climatology*, 38, 2994–3012, <https://doi.org/https://doi.org/10.1002/joc.5478>, 2018a.
- Pokhrel, S., Hazra, A., Saha, S. K., Chaudhari, H. S., Metya, A., Ghude, S. D., and Konwar, M.: Contrast in monsoon precipitation over oceanic region of north Bay of Bengal and east equatorial Indian Ocean, *International Journal of Climatology*, 38, e1061–e1075, 955 <https://doi.org/https://doi.org/10.1002/joc.5433>, 2018b.
- Ponukumati, P., Mohammed, A., and Regonda, S.: Insights on Satellite-Based IMERG Precipitation Estimates at Multiple Space and Time Scales for a Developing Urban Region in India, *Journal of Hydrometeorology*, 24, 977 – 996, <https://doi.org/10.1175/JHM-D-22-0160.1>, 2023.
- Pothapakula, P. K., Prein, A. F., Sunkisala, A., and Dipankar, A.: Global Monsoon in ICON: The Scale-Dependent Response of Northern 960 Hemisphere Monsoons, *EGUsphere*, 2026, 1–41, <https://doi.org/10.5194/egusphere-2026-782>, 2026.
- Prajeesh, A. G., Swapna, P., Krishnan, R., et al.: The Indian summer monsoon and Indian Ocean Dipole connection in the IITM Earth System Model (IITM-ESM), *Climate Dynamics*, 58, 1877–1897, <https://doi.org/10.1007/s00382-021-05999-z>, 2022.
- Prakash, S. and Srinivasan, J.: A Comprehensive Evaluation of Near-Real-Time and Research Products of IMERG Precipitation over India for the Southwest Monsoon Period, *Remote Sensing*, 13, <https://doi.org/10.3390/rs13183676>, 2021.
- 965 Prein, A. F., Langhans, W., Fosser, G., Ferrone, A., Ban, N., Goergen, K., Keller, M., Tölle, M., Gutjahr, O., Feser, F., Brisson, E., Kollet, S., Schmidli, J., van Lipzig, N. P. M., and Leung, R.: A review on regional convection-permitting climate modeling: Demonstrations, prospects, and challenges, *Reviews of Geophysics*, 53, 323–361, <https://doi.org/10.1002/2014RG000475>, 2015.
- Prein, A. F., Pothapakula, P., Zeman, C., Lalonde, M., and Rixen, M.: From Single Storms to Global Waves: A Global 2.5 km ICON Simulation of Weather and Climate, *EGUsphere*, 2026, 1–34, <https://doi.org/10.5194/egusphere-2025-6414>, 2026.
- 970 Rajendran, K., Surendran, S., Varghese, S. J., and Sathyanath, A.: Simulation of Indian summer monsoon rainfall, interannual variability and teleconnections: evaluation of CMIP6 models, *Climate Dynamics*, 58, 2693–2723, <https://doi.org/10.1007/s00382-021-06027-w>, 2022.
- Raschendorfer, M., Simmer, C., and Gross, P.: Parameterisation of Turbulent Transport in the Atmosphere, pp. 167–185, Springer Berlin Heidelberg, Berlin, Heidelberg, ISBN 978-3-540-45256-0, https://doi.org/10.1007/3-540-45256-7_10, 2003.



- Rio, C., Hourdin, F., Grandpeix, J.-Y., and Lafore, J.-P.: Shifting the diurnal cycle of parameterized deep convection over land, *Geophysical Research Letters*, 36, <https://doi.org/https://doi.org/10.1029/2008GL036779>, 2009.
- Saha, S. K., Pokhrel, S., Chaudhari, H. S., Dhakate, A., Shewale, S., Sabeerali, C. T., Salunke, K., Hazra, A., Mahapatra, S., and Rao, A. S.: Improved simulation of Indian summer monsoon in latest NCEP climate forecast system free run, *International Journal of Climatology*, 34, 1628–1641, <https://doi.org/https://doi.org/10.1002/joc.3791>, 2014.
- Sahany, S.: Fine-Scale Structure of Diurnal Variations of Indian Monsoon Rainfall: Observational Analysis and Numerical Modeling, PhD thesis, Centre for Atmospheric and Oceanic Sciences, Indian Institute of Science, Bangalore, India, 2009.
- Sahany, S., Venugopal, V., and Nanjundiah, R. S.: Diurnal-scale signatures of monsoon rainfall over the Indian region from TRMM satellite observations, *Journal of Geophysical Research: Atmospheres*, 115, <https://doi.org/https://doi.org/10.1029/2009JD012644>, 2010.
- Satoh, M., Matsuno, T., Tomita, H., Miura, H., Nasuno, T., and Iga, S.: Nonhydrostatic icosahedral atmospheric model (NICAM) for global cloud resolving simulations, *Journal of Computational Physics*, 227, 3486–3514, <https://doi.org/https://doi.org/10.1016/j.jcp.2007.02.006>, 2008.
- Schulz, J.-P. and Vogel, G.: Improving the Processes in the Land Surface Scheme TERRA: Bare Soil Evaporation and Skin Temperature, *Atmosphere*, 11, <https://doi.org/10.3390/atmos11050513>, 2020.
- Seifert, A.: On the Parameterization of Evaporation of Raindrops as Simulated by a One-Dimensional Rainshaft Model, *Journal of the Atmospheric Sciences*, 65, 3608 – 3619, <https://doi.org/10.1175/2008JAS2586.1>, 2008.
- Sen Roy, S. and Balling Jr., R. C.: Diurnal variations in summer season precipitation in India, *International Journal of Climatology*, 27, 969–976, <https://doi.org/https://doi.org/10.1002/joc.1458>, 2007.
- Seo, H., Subramanian, A. C., Miller, A. J., and Cavanaugh, N. R.: Coupled Impacts of the Diurnal Cycle of Sea Surface Temperature on the Madden–Julian Oscillation, *Journal of Climate*, 27, 8422 – 8443, <https://doi.org/10.1175/JCLI-D-14-00141.1>, 2014.
- Shukla, J.: Interannual variability of monsoons, *Monsoons*, pp. 523–548, 1987.
- Sikka, D. R.: Some aspects of the life history, structure and movement of monsoon depressions, *pure and applied geophysics*, 115, 1501–1529, <https://doi.org/10.1007/BF00874421>, 1977.
- Sikka, D. R. and Gadgil, S.: On the Maximum Cloud Zone and the ITCZ over Indian Longitudes during the Southwest Monsoon, *Monthly Weather Review*, 108, 1840 – 1853, [https://doi.org/10.1175/1520-0493\(1980\)108<1840:OTMCZA>2.0.CO;2](https://doi.org/10.1175/1520-0493(1980)108<1840:OTMCZA>2.0.CO;2), 1980.
- Singh, C.: Intra-seasonal oscillations of South Asian summer monsoon in coupled climate model cohort CMIP6, *Climate Dynamics*, 60, 179–199, <https://doi.org/10.1007/s00382-022-06323-z>, 2023.
- Sperber, K. R., Annamalai, H., Kang, I. S., Kitoh, A., Moise, A., Turner, A., Wang, B., and Zhou, T.: The Asian summer monsoon: an inter-comparison of CMIP5 vs. CMIP3 simulations of the late 20th century, *Climate Dynamics*, 41, 2711–2744, <https://doi.org/10.1007/s00382-012-1607-6>, 2013.
- Stephens, G. L., L’Ecuyer, T., Forbes, R., Gettelmen, A., Golaz, J.-C., Bodas-Salcedo, A., Suzuki, K., Gabriel, P., and Haynes, J.: Dreary state of precipitation in global models, *Journal of Geophysical Research: Atmospheres*, 115, <https://doi.org/https://doi.org/10.1029/2010JD014532>, 2010.
- Stevens, B., Giorgetta, M., Esch, M., Mauritsen, T., Crueger, T., Rast, S., Salzmann, M., Schmidt, H., Bader, J., Block, K., Brokopf, R., Fast, I., Kinne, S., Kornbluh, L., Lohmann, U., Pincus, R., Reichler, T., and Roeckner, E.: Atmospheric component of the MPI-M Earth System Model: ECHAM6, *Journal of Advances in Modeling Earth Systems*, 5, 146–172, <https://doi.org/https://doi.org/10.1002/jame.20015>, 2013.
- Stevens, B., Satoh, M., Auger, L., Biercamp, J., Bretherton, C., Chen, X., Durran, D., Emanuel, K., Fu, Q., Griffiths, M., Haerter, J. O., Heus, T., Heymsfield, A., Hong, S.-J., Khairoutdinov, M., Klocke, D., Mellado, J. P., Miltenberger, A., Noda, A. T., Pauluis, O., Rio, C.,



- Roehrig, R., Sato, Y., Sugi, M., van Ulft, L., Yamada, Y., and Zhou, C.: DYAMOND: the DYnamics of the Atmospheric general circulation Modeled On Non-hydrostatic Domains, *Progress in Earth and Planetary Science*, 6, 61, <https://doi.org/10.1186/s40645-019-0304-z>, 2019.
- 1015 Swapna, P., Krishnan, R., Sandeep, N., Prajeesh, A. G., Ayantika, D. C., Manmeet, S., and Vellore, R.: Long-Term Climate Simulations Using the IITM Earth System Model (IITM-ESMv2) With Focus on the South Asian Monsoon, *Journal of Advances in Modeling Earth Systems*, 10, 1127–1149, <https://doi.org/https://doi.org/10.1029/2017MS001262>, 2018.
- Tang, S., Gleckler, P., Xie, S., Lee, J., Ahn, M.-S., Covey, C., and Zhang, C.: Evaluating the Diurnal and Semidiurnal Cycle of Precipitation in CMIP6 Models Using Satellite- and Ground-Based Observations, *Journal of Climate*, 34, 3189 – 3210, <https://doi.org/10.1175/JCLI-D-20-0639.1>, 2021.
- 1020 Tang, S., Xie, S., Guo, Z., Hong, S.-Y., Khouider, B., Klocke, D., Köhler, M., Koo, M.-S., Krishna, P. M., Larson, V. E., Park, S., Vailancourt, P. A., Wang, Y.-C., Yang, J., Daleu, C. L., Homeyer, C. R., Jones, T. R., Malap, N., Neggers, R., Prabhakaran, T., Ramirez, E., Schumacher, C., Tao, C., Bechtold, P., Ma, H.-Y., Neelin, J. D., and Zeng, X.: Long-term single-column model intercomparison of diurnal cycle of precipitation over midlatitude and tropical land, *Quarterly Journal of the Royal Meteorological Society*, 148, 641–669, <https://doi.org/https://doi.org/10.1002/qj.4222>, 2022.
- 1025 Tao, C., Xie, S., Tang, S., et al.: Diurnal cycle of precipitation over global monsoon systems in CMIP6 simulations, *Climate Dynamics*, 60, 3947–3968, <https://doi.org/10.1007/s00382-022-06546-0>, 2023.
- Tatebe, H., Ogura, T., Nitta, T., Komuro, Y., Ogochi, K., Takemura, T., Sudo, K., Sekiguchi, M., Abe, M., Saito, F., Chikira, M., Watanabe, S., Mori, M., Hirota, N., Kawatani, Y., Mochizuki, T., Yoshimura, K., Takata, K., O’ishi, R., Yamazaki, D., Suzuki, T., Kurogi, M., Kataoka, T., Watanabe, M., and Kimoto, M.: Description and basic evaluation of simulated mean state, internal variability, and climate sensitivity in MIROC6, *Geoscientific Model Development*, 12, 2727–2765, <https://doi.org/10.5194/gmd-12-2727-2019>, 2019.
- 1030 Tawfik, A. B., Lawrence, D. M., and Dirmeyer, P. A.: Representing subgrid convective initiation in the Community Earth System Model, *Journal of Advances in Modeling Earth Systems*, 9, 1740–1758, <https://doi.org/https://doi.org/10.1002/2016MS000866>, 2017.
- Taylor, K. E., Williamson, D., and Zwiers, F.: The sea surface temperature and sea ice concentration boundary conditions for AMIP II simulations, Tech. Rep. PCMDI Report 60, Program for Climate Model Diagnosis and Intercomparison, Lawrence Livermore National Laboratory, <https://pcmdi.llnl.gov/report/pdf/60.pdf?id=86>, accessed 2026, 2000.
- 1035 Tiedtke, M.: A Comprehensive Mass Flux Scheme for Cumulus Parameterization in Large-Scale Models, *Monthly Weather Review*, 117, 1779 – 1800, [https://doi.org/10.1175/1520-0493\(1989\)117<1779:ACMFSF>2.0.CO;2](https://doi.org/10.1175/1520-0493(1989)117<1779:ACMFSF>2.0.CO;2), 1989.
- Torrence, C. and Compo, G. P.: A Practical Guide to Wavelet Analysis, *Bulletin of the American Meteorological Society*, 79, 61 – 78, [https://doi.org/10.1175/1520-0477\(1998\)079<0061:APGTWA>2.0.CO;2](https://doi.org/10.1175/1520-0477(1998)079<0061:APGTWA>2.0.CO;2), 1998.
- 1040 Trenberth, K. E., Dai, A., Rasmussen, R. M., and Parsons, D. B.: The Changing Character of Precipitation, *Bulletin of the American Meteorological Society*, 84, 1205 – 1218, <https://doi.org/10.1175/BAMS-84-9-1205>, 2003.
- Turner, A. G. and Annamalai, H.: Climate change and the South Asian summer monsoon, *Nature Climate Change*, 2, 587–595, <https://doi.org/10.1038/nclimate1495>, 2012.
- 1045 Voldoire, A.: CNRM-CERFACS CNRM-CM6-1-HR model output prepared for CMIP6 CMIP amip, <https://doi.org/10.22033/ESGF/CMIP6.3923>, 2019.
- Voldoire, A., Saint-Martin, D., Sénési, S., Decharme, B., Alias, A., Chevallier, M., Colin, J., Guérémy, J.-F., Michou, M., Moine, M.-P., Nabat, P., Roehrig, R., Salas y Méliá, D., Séférián, R., Valcke, S., Beau, I., Belamari, S., Berthet, S., Cassou, C., Cattiaux, J., Deshayes, J., Douville, H., Ethé, C., Franchistéguy, L., Geoffroy, O., Lévy, C., Madec, G., Meurdesoif, Y., Msadek, R., Ribes, A., Sanchez-Gomez,



- E., Terray, L., and Waldman, R.: Evaluation of CMIP6 DECK Experiments With CNRM-CM6-1, *Journal of Advances in Modeling Earth Systems*, 11, 2177–2213, <https://doi.org/https://doi.org/10.1029/2019MS001683>, 2019.
- 1050
- Waliser, D. E., Jin, K., Kang, I.-S., et al.: AGCM simulations of intraseasonal variability associated with the Asian summer monsoon, *Climate Dynamics*, 21, 423–446, <https://doi.org/10.1007/s00382-003-0337-1>, 2003.
- Wan, H., Giorgetta, M. A., Zängl, G., Restelli, M., Majewski, D., Bonaventura, L., Fröhlich, K., Reinert, D., Rípodas, P., Kornbluh, L., and Förstner, J.: The ICON-1.2 hydrostatic atmospheric dynamical core on triangular grids-Part 1: Formulation and performance of the baseline version, *Geoscientific Model Development*, 6, 735–763, <https://doi.org/10.5194/gmd-6-735-2013>, 2013.
- 1055
- Wang, B.: *The Asian Monsoon*, Springer Praxis Books, Springer, Berlin, Heidelberg, ISBN 978-3-540-37722-1, <https://doi.org/10.1007/3-540-37722-0>, 2006.
- Watters, D., Battaglia, A., and Allan, R. P.: The Diurnal Cycle of Precipitation according to Multiple Decades of Global Satellite Observations, Three CMIP6 Models, and the ECMWF Reanalysis, *Journal of Climate*, 34, 5063 – 5080, <https://doi.org/10.1175/JCLI-D-20-0966.1>,
- 1060
- 2021.
- Webster, P. J., Magaña, V. O., Palmer, T. N., Shukla, J., Tomas, R. A., Yanai, M., and Yasunari, T.: Monsoons: Processes, predictability, and the prospects for prediction, *Journal of Geophysical Research: Oceans*, 103, 14 451–14 510, <https://doi.org/https://doi.org/10.1029/97JC02719>, 1998.
- Wheeler, M. and Kiladis, G. N.: Convectively Coupled Equatorial Waves: Analysis of Clouds and Temperature in the Wavenumber–Frequency Domain, *Journal of the Atmospheric Sciences*, 56, 374 – 399, [https://doi.org/10.1175/1520-0469\(1999\)056<0374:CCEWAO>2.0.CO;2](https://doi.org/10.1175/1520-0469(1999)056<0374:CCEWAO>2.0.CO;2), 1999.
- 1065
- Yang, G.-Y. and Slingo, J.: The Diurnal Cycle in the Tropics, *Monthly Weather Review*, 129, 784 – 801, [https://doi.org/10.1175/1520-0493\(2001\)129<0784:TDCITT>2.0.CO;2](https://doi.org/10.1175/1520-0493(2001)129<0784:TDCITT>2.0.CO;2), 2001.
- Yasunari, T.: Cloudiness Fluctuations Associated with the Northern Hemisphere Summer Monsoon, *Journal of the Meteorological Society of Japan. Ser. II*, 57, 227–242, https://doi.org/10.2151/jmsj1965.57.3_227, 1979.
- 1070
- Zhang, B., Donner, L. J., Zhao, M., and Tan, Z.: Improved Precipitation Diurnal Cycle in GFDL Climate Models With Non-Equilibrium Convection, *Journal of Advances in Modeling Earth Systems*, 16, e2024MS004 315, <https://doi.org/https://doi.org/10.1029/2024MS004315>, 2024.
- Zhao, Q. and Carr, F. H.: A Prognostic Cloud Scheme for Operational NWP Models, *Monthly Weather Review*, 125, 1931 – 1953, [https://doi.org/10.1175/1520-0493\(1997\)125<1931:APCSFO>2.0.CO;2](https://doi.org/10.1175/1520-0493(1997)125<1931:APCSFO>2.0.CO;2), 1997.
- 1075
- Zhou, T., Yu, R., Chen, H., Dai, A., and Pan, Y.: Summer Precipitation Frequency, Intensity, and Diurnal Cycle over China: A Comparison of Satellite Data with Rain Gauge Observations, *Journal of Climate*, 21, 3997 – 4010, <https://doi.org/10.1175/2008JCLI2028.1>, 2008.
- Zängl, G., Reinert, D., Rípodas, P., and Baldauf, M.: The ICON (ICOsahedral Non-hydrostatic) modelling framework of DWD and MPI-M: Description of the non-hydrostatic dynamical core, *Quarterly Journal of the Royal Meteorological Society*, 141, 563–579, <https://doi.org/https://doi.org/10.1002/qj.2378>, 2015.
- 1080